



## Geochemical and mineralogical differences between supergene and hypogene gold mineralization and influence on gold recovery: A case study of the Faina gold deposit, Pitangui greenstone belt, Brazil

Gabriel Machado da Silva<sup>1</sup> ; Atlas Vasconcelos Corrêa Neto<sup>2</sup> ; Mariana Brando Soares<sup>3</sup> ; Felipe Emerson André Alves<sup>4</sup> ; Nicollas de Oliveira Ferreira Santos<sup>2</sup> ; Piero Azevedo Berquó de Sampaio<sup>2,6,7</sup> ; Vitor Diniz Silveira<sup>5</sup> , Gabriel Faria Gonçalves<sup>5</sup> 

<sup>1</sup>Universidade Federal do Rio de Janeiro - UFRJ Programa de Pós-Graduação em Geologia-PPGL, Av. Athos da Silveira Ramos, 274, Cidade Universitária, Rio de Janeiro - RJ, Brazil, CEP: 21941-909

<sup>2</sup>Universidade Federal do Rio de Janeiro - UFRJ, Av. Athos da Silveira Ramos, 274, Cidade Universitária, Rio de Janeiro - RJ, Brazil, CEP: 21941-909

<sup>3</sup>Universidade Estadual do Rio de Janeiro - UERJ, Rua São Francisco Xavier, 524, Maracanã, Rio de Janeiro, RJ, Brazil, CEP: 20550-013

<sup>4</sup>Centro de Tecnologia Mineral - CETEM, Av. Pedro Calmon, 900, Cidade Universitária, Rio de Janeiro - RJ, Brazil, CEP: 21941-908

<sup>5</sup>Jaguar Mining Inc., Rua Andaluzita, 131, Carmo, Belo Horizonte - MG, Brazil, CEP: 30310-030

<sup>6</sup>Curtin University, Earth Dynamics Research Group (EDRG), School of Earth and Planetary Sciences, Kent St, Bentley WA 6102, Perth, WA, Australia.

<sup>7</sup>Earth Evolution and Dynamics Research Center (EDRC), Laoshan Laboratory, Qingdao, 266237, China.

### Abstract

The Faina gold deposit, located in the Pitangui Greenstone Belt, NW of the Quadrilátero Ferrífero, Brazil, has produced gold from the oxidized portion of the deposit between June 2010 and June 2013. However, the deeper hypogene (sulfide-rich) section of the deposit has shown lower-than-expected recovery rates after direct leaching, leading to the interruption of gold production. This research presents a multi-methodological approach (drill core description, multi-element geochemical analyses and mineral characterization using microscopy and X-ray diffraction) to investigate describe the Faina gold deposit and identify the cause of low recoveries from the hypogene zone. The stratigraphy at Faina consists of a sequence of meta-mafic and meta-sedimentary rocks with a thick (>40m) saprolite horizon (oxidized portion). Both the meta-mafic rocks and saprolite host gold mineralization, which is identified by distinct geochemical and mineral signatures: 1) Au-As-W in the hypogene zone, with gold associated with sulfides or as disseminations in silicates and 2) Au-As-W in the oxide-rich shallower section with free-milling gold associated with quartz, iron oxide-hydroxides and clay minerals. Geochemical, mineral and textural relationships in the hypogene zone show that submicroscopic gold particles associated with minerals that consume leaching solution minerals (arsenopyrite, pyrrhotite and berthierite) may cause refractoriness during direct leaching. Separation of gold from these mineral phases, in addition to concentration methods during ore processing may increase gold recovery. The results presented in this research emphasize the importance of a detailed geochemical and mineral characterization to reveal the contrasting mineral and chemical compositions between hypogene and oxidized zone, which may influence gold recovery.

### Article Information

Publication type: Research Papers  
Received 10 September 2024  
Accepted 2 January 2025  
Online pub. 7 January 2025  
Editor: E. Klein

**Keywords:**  
Pitangui greenstone belt  
Faina deposit  
Gold recovery  
Mineral processing

\*Corresponding author  
Gabriel machado da Silva  
E-mail address: [gabrielgms2204@gmail.com](mailto:gabrielgms2204@gmail.com)

### 1. Introduction

Understanding the mineralogical and geochemical characteristics of ore deposits is a crucial aspect of the ore beneficiation process, as these characteristics are directly linked to metal recovery during ore processing (Feng and Van Deventer 2010; Lang et al. 2018; Costa et al. 2022). This information can be used in predictive metallurgy (Silva-Alves et al. 2022) by providing early-stage insights into possible future ore processing flowcharts. Additionally, the

understanding of the genesis of mineral deposits is further improved through such studies (Mano et al. 2020; Alves et al. 2022), leading to beneficial feedback cycles between academy and industry to develop more accurate exploration models and predictive metallurgy.

Refractory gold refers to materials with low recovery rates in direct cyanidation methods, resulting in high cyanide consumption to extract the gold (Komnitsas and Pooley 1989). Refractory gold is caused by multiple factors, which include:

i) Physical locking, where fine-grained or submicroscopic gold particles (less than 10  $\mu\text{m}$ ) are trapped within sulfides such as arsenopyrite or pyrite making the gold unavailable to react with the cyanide solution (Swash 1988; Komnitsas and Pooley 1989; Vaughan 2004);

ii) Chemical locking, in which mineral phases or complex alloys containing gold atoms (i.e. gold tellurides) or the presence of submicroscopic (nano size) gold atoms occur within the crystalline lattice of sulfides

iii) presence of cyanicides (cyanide-consuming elements) and leaching robbing minerals, such as sulfides (e.g., pyrrhotite, arsenopyrite, berthierite and stibnite) whose decomposition reaction consume oxygen and/or cyanide ions. (Komnitsas and Pooley 1989; Bulatovic and Wyslouzil 2000; Vaughan 2004; Adams 2016; Chryssoulis and McMullen 2016; Rohner and Millard 2016).

iv) Preg-robbing ores: usually fine-grained material, like carbonaceous mud which adsorbs gold and prevents its capture by cyanide

The oxidized section of the Faina gold deposit, located in the Pitangui Greenstone Belt (PGB), NW of the Quadrilátero Ferrífero (QF, Figure 1B), was operated intermittently between 2010 and 2013 (Pressaco et al. 2022) using the processing plant of the Turmalina Mine Complex (Pressaco et al. 2022). The hypogene zone of the Faina deposit, characterized by sulfide enrichment, showed recovery results lower than expected and therefore production was halted in 2013 (Pressaco et al. 2022). A recent, intense brownfield exploration program, has revealed the Mineral Reserves at the Faina deposit to be about 787.000 t at an average grade of 5.22g/t containing 132.000 oz Au (Probable Mineral Reserves). Mineral Resources were estimated to be about 1.427.000 t at an average grade of 5.08 g/t containing 233.000z oz Au (Measured and Indicated Mineral Resource) and 1.420.000 t at an average grade of 5,09 g/t containing 232.000 oz Au (Inferred Mineral Resource) (Jaguar Mining 2023).

According to Pressaco et al. (2022), direct cyanidation tests in the oxidized portion of the Faina deposit resulted in an average gold extraction of 96.1% from samples with approximately 83% passing minus 200 mesh (74 $\mu\text{m}$ ). In contrast, similar tests performed on samples from hypogene portion resulted in an average gold extraction of 42.91% at 80% passing minus 200 mesh (74 $\mu\text{m}$ ) and an average gold extraction of 42.99% at 80% passing minus 270 mesh (53 $\mu\text{m}$ ). The results therefore shows that gold mineralization in the hypogenic section of the Faina deposit presents recovery challenges.

In a previous study, Pressaco et al. 2022 conducted metallurgical tests on two composite samples to determine the best treatment route for the Faina gold ores. Relatively better results for the first set of samples were achieved with gravimetric concentration followed by flotation with 80% passing minus 270 mesh (53 $\mu\text{m}$ ), where the gold recovery ranged from 88.02 and 92.36%. For the second set of samples, better results were obtained using flotation with 80% passing minus 270 mesh (53 $\mu\text{m}$ ), where the gold recoveries ranged from 87.21 and 89.72%.

In this work, we present the results of combined mineralogical and geochemical investigations of the Faina deposit through conventional reflected light petrographic studies, SEM-EDS, X-ray diffraction and multivariate statistical analysis. The results here were used to characterize

the gold deposit to provide an understanding of the factors that control the poor recovery from the ore. Another study was also undertaken to investigate the effect of weathering on gold liberation from sulfides. The findings of this study can be used to develop new workflows and flowsheets for mining and exploration projects by incorporating data derived from the above-cited methods, where improvement in efficiency and/or predictability of gold recovery can be expected in current operations. Mineral exploration projects, in turn, will benefit from more precise forecasts, leading to better tailored routes for optimal gold recovery performance.

## 2. Regional Geological Setting

The Pitangui greenstone belt is part of the *Quadrilátero Ferrífero* metallogenic province, which hosts world-class gold deposits such as the Cuiabá and Morro Velho gold deposits (Dorr 1969; Lobato et al. 2001a; Lobato et al. 2001b; Ribeiro-Rodrigues et al. 2007; Vial et al. 2007). The *Quadrilátero Ferrífero* is located at the southern portion of the São Francisco Craton and comprises a basement made up of Meso- to Neoproterozoic granite-gneiss terrains and Meso- to Neoproterozoic metavolcanosedimentary sequences (Figure 1A). The basement is overlain by Proterozoic metasedimentary sequences which include Minas Supergroup, Espinhaço Supergroup, (Dorr 1969; Machado and Carneiro 1992; Lobato et al. 2001a; Baltazar and Zuccheti 2007; Baltazar and Lobato 2020) and the Bambuí Group (Zalán and Romeiro-Silva 2007).

The granite-gneiss terrains consist of orthogneisses with a trondhjemite-tonalite-granite signature, migmatites and intrusive granitoids metamorphosed at upper amphibolite facies exposed as dome-like structures (Teixeira et al. 1996; Lana et al. 2013). These rocks are associated with three magmatic events (Lana et al. 2013): (i) Santa Barbara (3.220 - 3.200 Ma); (ii) Rio das Velhas I (2930 – 2900 Ma) and Rio das Velhas II (2800 – 2760 Ma). The metavolc-sedimentary belts are represented by Rio das Velhas, Pitangui and Rio Manso greenstone belts (Dorr 1969; Baltazar and Zuccheti 2007; Lana et al. 2013; Brando Soares et al. 2017).

Three orogenic events have been documented to have affected the southern portion of the São Francisco Craton. The initial event is the Mesoarchean Campo Belo orogeny (3.05 – 2.92 Ga, Teixeira et al. 2017), which affected the TTG-gneiss terrains. This was followed by the Neoproterozoic Rio das Velhas orogeny (2.78Ga – 2.70Ga, Carneiro 1992; Baltazar and Zuccheti 2007). Both events affected the granite-gneiss terrains and metavolcanic-sedimentary greenstone belts. The third event is the Rhyacian-Orosirian orogeny (2.4 – 2.1 Ga, Alkmim and Marshak 1998; Teixeira et al. 2015; Alkmim and Teixeira 2017; Bruno et al. 2020; Bruno et al. 2021). The effects of Neoproterozoic Brasiliano orogeny are restricted to the easternmost sectors of the Quadrilátero Ferrífero.

### 2.1. Local geology

The Pitangui greenstone belt (PGB) is a Neoproterozoic metavolcanic-sedimentary rock succession located northwest to the QF (Figure 1). It comprises a NW-SE synclinorium, bounded by the TTG Divinópolis and Belo Horizonte complexes domes (Figure 1A) and younger Neoproterozoic granite intrusions (2755Ma – 2711Ma) (Romano 2007; Brando Soares et al. 2017; Marinho et al. 2018; Melo-Silva et al. 2020).

The lithostratigraphy of the PGB encompasses two main units (Marinho et al. 2018): the basal Pitangui Group and the Antimes Formation. The former is subdivided into three units, from bottom to top: Rio Pará, Rio São João and Onça de Pitangui Formations. The Rio Pará Formation (2.88Ga; Marinho et al. 2018) consists of meta-basalts overlain by quartzite, meta-cherts, BIFs and phyllites. The Rio São João Formation (2765Ma, U-Pb maximum depositional age, Brando Soares et al. 2017) is characterized by an intercalation of meta-rhytmities, meta-basalts, meta-cherts, BIFs and quartzites. The Onça de Pitangui Formation comprises intercalations of meta-sandstones, BIFs, meta-cherts and metapelites. The Antimes Formation (2684Ma, U-Pb maximum depositional age, Marinho et al. 2018) is composed of quartzites with lenses of polymictic metaconglomerates.

Pressaco et al. (2022) identified two tectonic events, whereas Fabricio-Silva et al. (2018) described three deformational phases. According to Pressaco et al. (2022), the first phase ( $D_N$ ) created a penetrative tectonic cleavage ( $S_N$ ) while the second phase ( $D_{N+1}$ ) is interpreted as a mild regional deformation event, represented by pervasive micro-crenulation planes developed over ( $S_N$ ). On the other hand, Fabricio-Silva et al. (2018) indicated that the first event ( $D_1$ ) created a NW striking and NNE dipping regional isoclinal fold, with a correlated penetrative axial-planar foliation. The second event ( $D_2$ ) is marked by ductile shear zones, mineral and stretching lineation, boudins, pinch-and-swell structures, crenulation cleavage (striking from NNW-SSE to NNE-SSW and dipping to W) and crenulation lineation. Both events are interpreted to be correlated to the Neoproterozoic Rio das Velhas orogeny constrained between 2.75 and 2.67 Ga (Baltazar and Zuccheti 2007, 2020). The third event ( $D_3$ ) is represented by Paleoproterozoic left-lateral transpressional reactivation of Neoproterozoic SE-NW regional shear zones folding and reverse faulting.

## 2.2. Turmalina Mine Complex

The Turmalina Mine Complex (MTL, Figure 1B) consists of several gold orebodies including orebody A, orebody B orebody C and Faina (Pressaco et al. 2022). MTL's main production comes from orebodies A and C. Orebody A is comprised of two intersecting tabular bodies dipping to the NE. Orebody C consists of 26 tabular lenses located west-northwest from orebody A structural footwall. Gold at MTL is present as fine-grained grains associated with sulfides and quartz-veins within sheared schists and folded BIFs (Fabricio-Silva et al. 2018). The gold deposits at MTL differ significantly from those in central QF as they are hosted higher metamorphic grade rocks (amphibolite facies) with a distinct geochemical signature that shows close association between gold, Sb and Bi.

## 3. Material and Methods

Materials provided by Jaguar Mining included geochemical data from nine drill cores (FUH-27, FUH-119, FUH-128, FUH-151, FUH-168, FUH-168A, FUH-169, FUH-170 and FUH-171), seven drill cores (FUH-27, FUH-119, FUH-128, FUH-151, FUH-168A, FUH-169 and FUH-171) for macroscopic description, sixty five pulps from intervals used for geochemistry assay for X-ray diffraction (XRD) analyses and ten polished sections for microscopic description.

### 3.1. Fieldwork

A detailed macroscopic description of seven drill cores (FUH-27, FUH-119, FUH-128, FUH-151, FUH-168A, FUH-169 and FUH-171) was conducted at the Jaguar Mining core shed in Conceição do Pará, MG, Brazil. The description focused on the identification of lithologies, hydrothermal alteration, and mineral assemblages of the sulfide-rich mineralized intervals in the hypogene portion of the deposit. Figure 1B shows the location and spatial distribution of the nine drill cores.

### 3.2. Multi-element analyses

Multi-element analyses of 49 elements were conducted at the ALS Global facility in Lima, Peru. Mineralized and non-mineralized intervals were sampled from the nine drill cores (FUH-27, FUH-119, FUH-128, FUH-151, FUH-168, FUH-168A, FUH-169, FUH-170 and FUH-171), yielding a total of 897 analyses. Gold concentration was measured using fire assay method and atomic absorption (ALS method Au-AA23), while the other 48 elements (Ag, Al, As, Ba, Be, Bi, Ca, Cd, Ce, Co, Cr, Cs, Cu, Fe, Ga, Ge, Hf, In, K, La, Li, Mg, Mn, Mo, Na, Nb, Ni, P, Pb, Rb, Re, S, Sb, Sc, Se, Sn, Sr, Ta, Te, Th, Ti, Tl, U, V, W, Y, Zn and Zr) were measured using the four-acid digestion technique with inductively coupled plasma mass spectrometry (ALS method ME-MS61).

The geochemical data was initially divided into two groups based on drill core description: hypogene (fresh-rocks) and supergene (oxidized) samples. The data was interpreted with the use of downhole plots to visualize gold grade distribution and the correlation between gold and other elements. A probability distribution plot was created using Minitab software (Minitab) with samples having Au grades above the detection limit (Au > 0.005ppm). This procedure was employed to separate different populations based on gold grade. Samples with low Au grades (Au values < 0.63ppm, Figure 2) were considered as background.

Binary plot diagrams comparing Au grades with As, Bi, S, Sb and W were created to understand their correlation with Au. For each graph, samples with values below the detection limit and above the limit of quantification were removed. The detection limit is the lowest concentration of an analyte that can be detected with an acceptable level of reliability, while the quantification limit is the highest concentration that can be measured accurately.

### 3.3. Multivariate statistical analyses

Several authors (e.g., Grunsky 2010; Nude et al. 2012, Grunsky and Caritat 2019) have proposed the application of multivariate statistical methods to geochemical datasets to enhance the study of large multi-element geochemical datasets.

The multivariate statistical method applied here is called Principal Component Analysis (PCA). Its main advantage is the representation of complex multivariate data by reducing the datasets into a few diagrams, allowing for the recognition of geochemical associations that can then serve as the basis for geological interpretation (i. e. lithology, weathering or hydrothermal alteration) (Grunsky 2010; Nude et al. 2012; Grunsky and Caritat 2019).

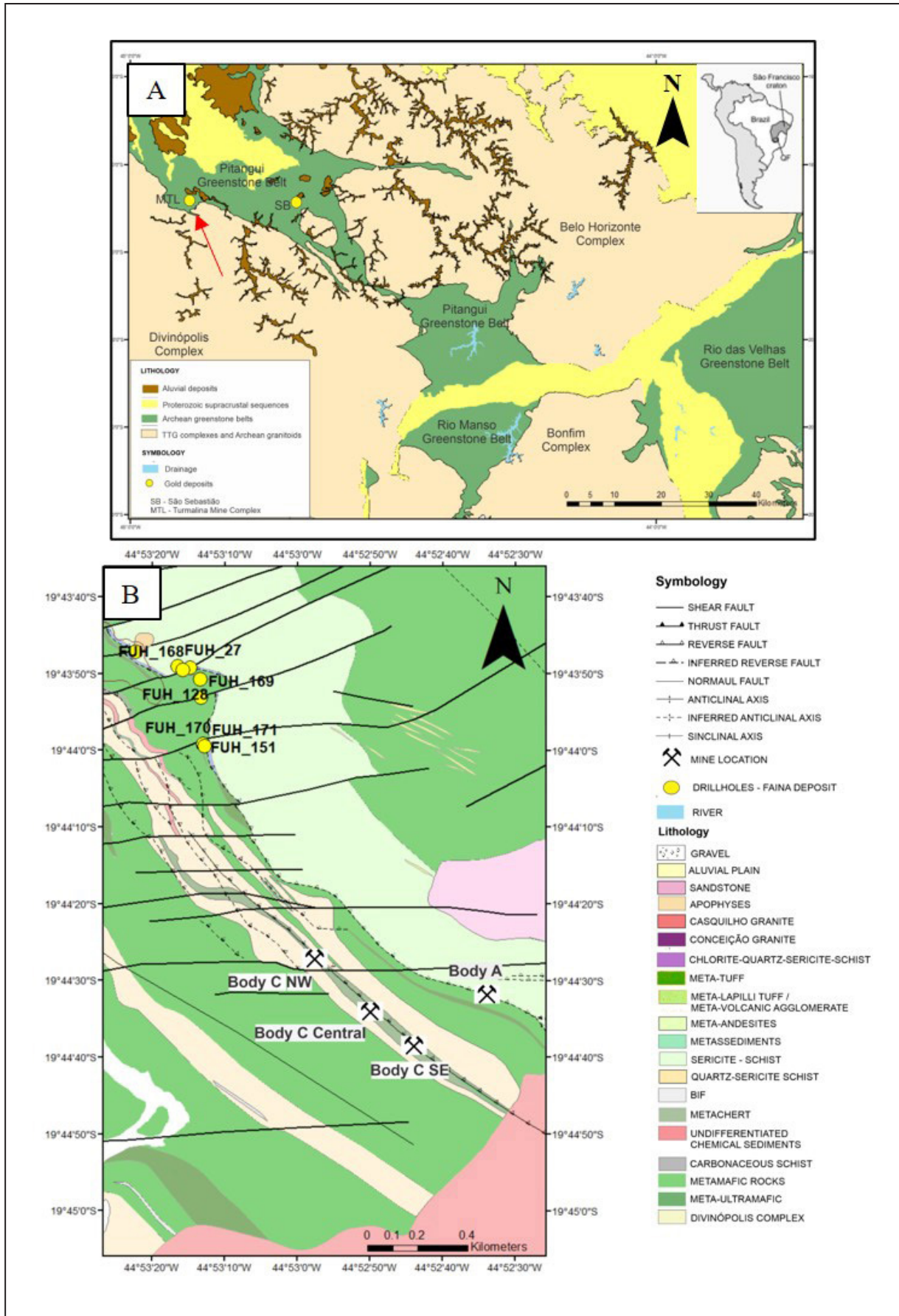
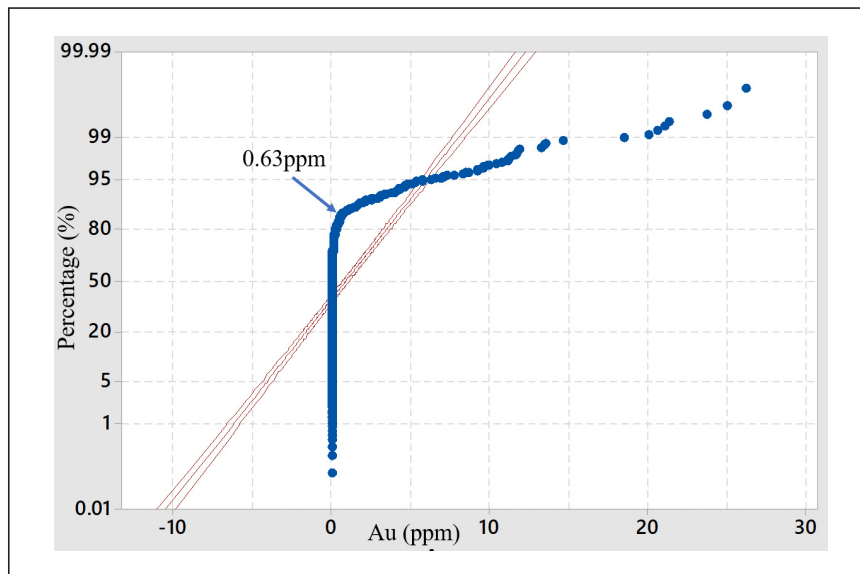


FIGURE 1. (A) Simplified regional geological map of Quadrilátero Ferrífero in the southern São Francisco Craton (SFC). Modified from Silva et al. (2020). Red arrow points to Turmalina Mine Complex. (B) Turmalina Mine Complex geological map. Modified from Silveira et al. (2021). Provided by Jaguar Mining. Red arrow points to Faina deposit.



**FIGURE 2.** Probability distribution diagram for Au grades. Samples with Au values above inflexion point (0.63ppm) were considered as mineralized samples, whereas samples with values below inflexion were considered as background.

For multivariate statistical analysis (Figure 10), assay results with gold grades below the detection limit and arsenic grades below the detection limit or above the limit of quantification were removed to ensure the analysis between samples with valid results for these variables.

### 3.3.1. Centered Log Ratio (CLR)

Prior to applying PCA, a CLR treatment was used to overcome the “closure problem” caused by expressing geochemical data as proportions, which can lead to unreliable statistical data and erroneous interpretations (Grunsky and Caritat 2019). Therefore, the CLR pre-treatment allows the application of traditional statistical methods (Aitchison 1986; Egozcue et al. 2003; Buccianti et al. 2006).

In addition to Au, results of Ag, As, Bi, Cr, Co, Cu, Mo, Ni, Pb, S, Sb, Te, Tl, W and Zn were selected for the CLR transformation. These elements were chosen because gold may or may not be associated with them, depending on the genesis of the deposit (Groves et al. 1998; Robb 2005; Hart 2007; Goldfarb and Groves 2015). The only exceptions are Cr and Ni, which were used as proxies for the host rock to evaluate chemical relationship between gold and the host rock. The transformation was performed with the ioGAS (IMDEX) software.

### 3.3.2. Principal Component Analyses (PCA)

Principal component analysis (PCA) was performed using ioGas software. PCA was applied to visualize the covariance among multiple elements simultaneously and to establish the main elements associated with gold mineralization (Grunsky 2010).

### 3.4. Major mineralogy determination and X-ray diffraction Rietveld method

Forty samples are from the hypogene zone, with 36 from mineralized intersections and 4 from non-mineralized

intervals. Since the focus was on the characterization of the mineralization, the only rock sampled for XRD analyses was the host rock, an actinolite-chlorite-schist, which is the sole rock hosting gold mineralization. The remaining 15 samples are from mineralized intervals of the oxidized zone.

Sample preparation, XRD analysis and Rietveld refinement were conducted at the Division for Mineral Characterization of Centre for Mineral Technology (CETEM), Brazil.

Approximately 3 grams of representative aliquots were sampled from each pulp powder sample using rotary splitters. The aliquots were ground for 10 minutes in a McCrone Micronizing Mill with an agate grinding media and 12 mL of deionized water. The milled samples were placed into PTFE Petri dishes and dried at 60°C under airflow for 24 hours. The dried samples were homogenized with agate mortar and pestle and then back loaded into sample holders.

Diffraction patterns were obtained on a Bruker-AXS D4 Endeavour diffractometer with  $k\beta$ -filtered Co K $\alpha$  radiation and a LynxEye position sensitive detector (PSD) in the range between 4° to 105° 2 $\theta$  with a step size 0.01°. Mineral identification was performed using Bruker-AXS's Diffra. Eva suite and PDF4+ 2017 database.

The Rietveld method-based mineral quantification, using a fundamental parameter approach (Cheary and Coelho 1992) was performed with Diffra.Topas 5.0 software. The background was automatically calculated using a 5th-order polynomial. Crystal structures used in the refinements were obtained from the Bruker Crystal Structure Database or the Crystallography Open Database (Grazulis et al. 2009).

Gold was not detected because it is below detection limit of this analytical technique.

### 3.5. Petrography and scanning electron microscope (SEM)

Ten samples from the hypogene mineralized intersections were prepared for petrography and scanning electron microscope (SEM) analysis. Eight polished sections were

examined using a reflected light microscope at the Laboratory of Petrology in the Rio de Janeiro State University (UERJ). Two polished sections were examined using a FEI Quanta 400 scanning electron microscope (SEM) coupled with a Bruker Quantax 800 energy-dispersive X-ray fluorescence spectroscope (EDS) with a Bruker XFlash 5010 silicon drift detector, and a Hitachi TM 3030 Plus coupled with a Bruker Quantax 70 EDS system. The FEI Quanta 400 SEM was operated at 20kV and a spot-size of 5 µm diameter, while the Hitachi TM 3030 Plus operated using the EDX mode. Both instruments are housed at CETEM.

The SEM analyses were conducted to identify the main mineral phases and textures related to mineralization.

## 4. Results

### 4.1. Stratigraphy of Faina deposit

The stratigraphy of the Faina deposit interpreted from drill core description and surface mapping is shown in Figure 3. The hypogene zone is predominantly composed of metavolcanic rocks interbedded with thin units of metasedimentary rocks to the base. The rocks are intensely affected by hydrothermal alteration, as evidenced by the presence of hydrothermal mineral phases. The oxidized zone is generally characterized by a red silty clay saprolite.

### 4.2. Lithologies

Five different lithologies were identified at Faina in this research. From the bottom to the top, these are carbonaceous phyllite (XG), meta-chert (MCH), amphibole-chlorite-schist (ACLX), talc-chlorite-schist (MVU) and biotite-amphibole-chlorite-schist (BACLX). At the top of this sequence, there is also a meta-conglomerate and biotite-schist unit, which are not present in the current study area, but have been described by other authors (Gonçalves et al. 2023; Silveira et al. 2023).

The carbonaceous phyllite (Figure 4G) is a strongly foliated sulfide-rich rock with the main phases being pyrite and pyrrhotite. The meta-chert (Figure 4F) is a compositionally banded rock with intercalated silica and iron-oxide laminae. The amphibole-chlorite schist (Figure 4E) is a dark-green color rock with the main foliation marked by oriented chlorite minerals and the mineral lineation marked by amphiboles. The talc-chlorite schist (Figure 4D) is composed mainly of talc, amphiboles and chlorite. The biotite-amphibole-chlorite-schist (Figure 4C) is a dark-green colored strongly foliated rock composed of brown-biotite, amphibole, and chlorite minerals. Meta-conglomerate is composed of deformed and oriented coarse-sized (pebble) grains with a fine-grained matrix (Figure 4B). The biotite-schist is a strongly foliated rock composed mainly by biotite with the presence of quartz-carbonate veins (Figure 4A). Biotite-schist (FUH211) and meta-conglomerate (FUH184) were not observed on the described drill holes. Photos from biotite-schist from drill hole core FUH211 and metaconglomerate from FUH184 were informed and provided by Jaguar Mining.

### 4.3. Hydrothermal Alterations

At Faina, four main hydrothermal alteration assemblages/patterns were identified. These include silicification, carbonate alteration, sulfidation and biotite alteration in order of abundance.

The silicification and carbonate alterations affect all lithologies and both alterations occur in the form of veins (Figure 5A). Three generations of quartz-carbonate veins were identified: the first generation occurs as boudins parallel to the main foliation. The second generation is discordant to the first generation, filling fractures at boudin necks and localized normal faults (Figure 5F). The third generation forms thicker veins that crosscut the main foliation with xenoliths of the host rock bearing either milky (Figure 5B) or smoky quartz (Figure 5C). The latter occurs more frequently near to or within high gold grade intersections and is associated with sulfides.

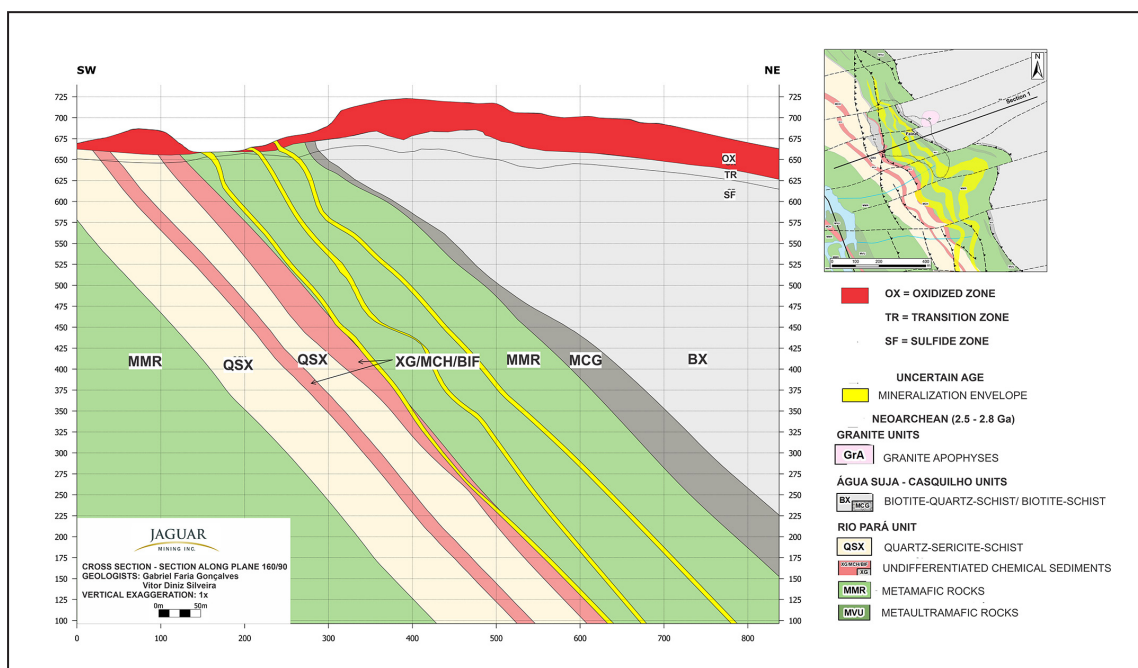
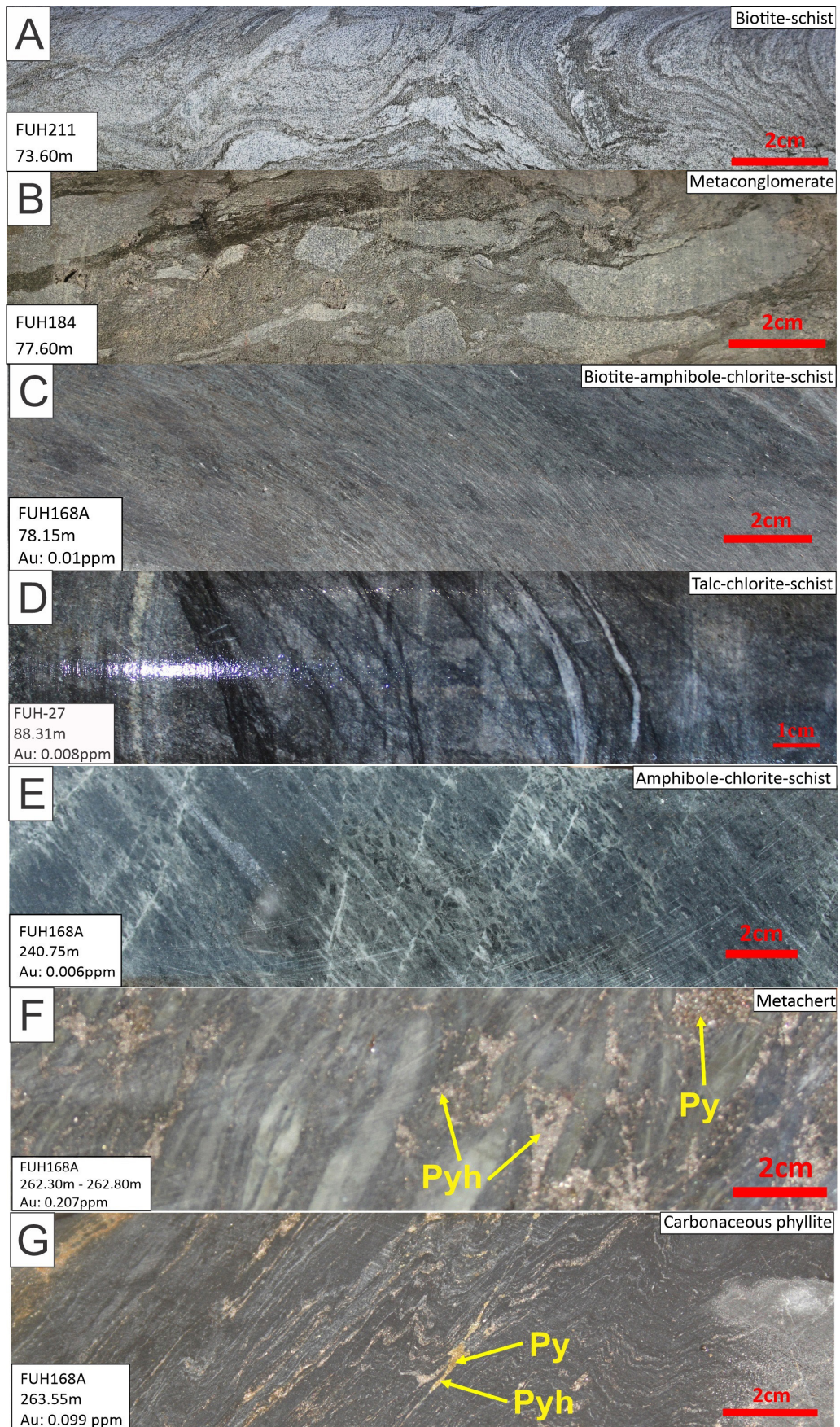


FIGURE 3. Schematic section of Faina deposit. Inset representing detailed geological map. Provided by Jaguar Mining.



**FIGURE 4.** Faina stratigraphy. (A) Biotite-schist. Photo provided by Jaguar Mining. (B) Metaconglomerate. Photo provided by Jaguar Mining. (C) Biotite-actinolite-chlorite-schist. (D) Talc-chlorite-schist. (E) Actinolite-chlorite-schist. (F) Metachert. (G) Carbon-rich phyllite. Py = pyrite. Pyh = pyrrhotite. Depth indicated in the pictures were measured from the top of the hole.

The biotite alteration consists of brown-fine-grained biotite crystals disseminated in the rock matrix and parallel to the main foliation (Figure 5D). This alteration affects only the meta- mafic rocks and is present near or within high-gold grade intervals, suggesting it interpreted as an alteration directly related to gold mineralization. Biotite alteration is also present at the borders of quartz-carbonate veins (Figure 5E) or parallel and spatially close to arsenopyrite veins (Figure 6A) and pyrrhotite veins (Figure 6C).

Sulfide alteration affects all lithologies. Arsenopyrite was observed as syn-tectonic crystals, while pyrrhotite and pyrite occur as both syn-tectonic and post-tectonic crystals. Minor phases, such as berthierite, chalcopyrite and sphalerite are post-tectonic minerals.

Arsenopyrite is restricted to high-gold grade intervals. Zones with millimetric to centimetric concentrations of fine-grained

arsenopyrite as well as disseminated flattened crystals aligned parallel to the main foliation occur in association with biotite alteration (Figure 6A). Arsenopyrite zones are not always spatially coincident with chalcopyrite- and pyrrhotite rich zones (Figure 6B). Syn-tectonic pyrrhotite (Figure 6C) occurs parallel to the main foliation disseminated among silicates and spatially close to biotite alteration zones. Post-tectonic pyrrhotite crystals occur in both high-gold grade and low-gold grade intervals. It is present in breccia zones (Figure 6D), associated with pyrite at the borders of dark-grey quartz veins (Figure 5E) or forming fracture-filling veinlets and lamellae with millimetric to centimetric thickness at quartz veins (Figure 6E). Pyrite occurs at both high- and low-grade intervals associated with quartz-carbonate veins filling fractures (Figure 6F) and at the borders of dark-grey quartz-vein in association with pyrrhotite (Figure 5E). Chalcopyrite crystals

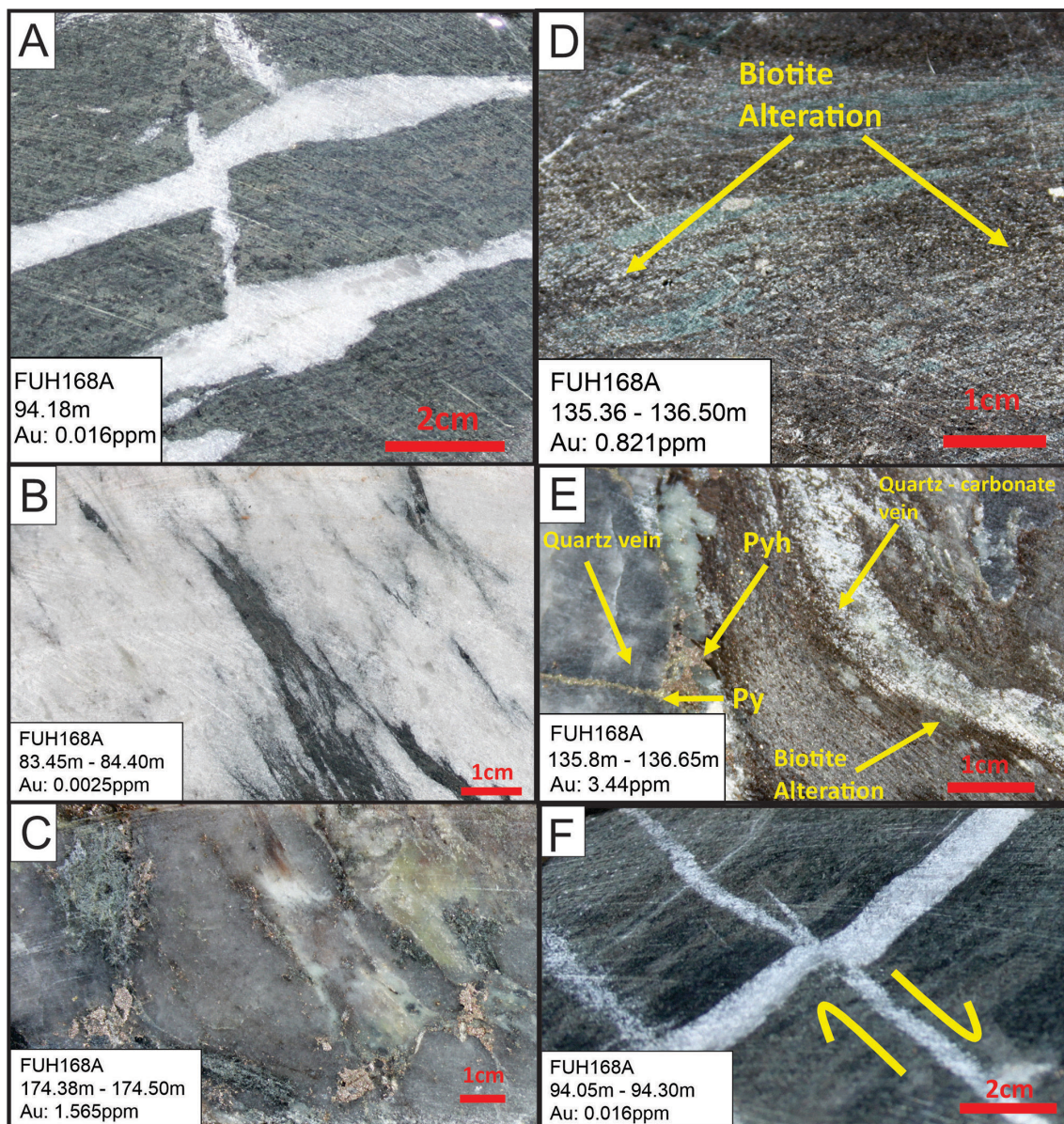


FIGURE 5. (A) Two generations of quartz carbonate veins. The first one parallel to the main foliation as boudins. The second orthogonal to the first generation, filling fractures at bouding necks. (B) Milky-white quartz vein with xenoliths of host rock. (C) Dark-grey quartz vein with xenoliths of host rock and sulfides, mainly pyrrhotite. (D) Biotite alteration. (E) Biotite alteration associated with quartz-carbonate veins and pyrrhotite (Pyh) and Pyrite (Py) at the border of veins. (F) Second generation of quartz-carbonate vein filling normal fault.

with borders of sphalerite, occur disseminated among silicate gangue and are associated with pyrrhotite (Figure 6G). Post-tectonic berthierite occurs as discordant veins associated with arsenopyrite veins (Figure 6H).

#### 4.4. Mineralized interval

High gold grade intervals are enclosed by silicification, sulfidation and biotitization halos. Quartz veins become more frequent near or at high-gold grades zones. Sulfide minerals identified at high-gold grade zones include arsenopyrite, pyrrhotite, pyrite, chalcopyrite, berthierite and sphalerite. Figure 7 shows the transition between barren host rock and the ore zone.

#### 4.5. Multi-element geochemistry

Gold anomalies spatially overlap with As, W, Sb, S and Bi in the FUH168A drillcore (Fig. 8). In the hypogene zone, gold anomalies were observed only within the meta-mafic units.

Binary plot diagrams from the hypogene zone (Figure 9A, C, E, G and I) reveal that gold shows a strong a strong positive correlation with As and a positive correlation with W and S. Au vs Sb and Bi diagram shows no correlation. Binary plot diagrams for the oxidized zone (Figure 9B, D, F, H and J) exhibit a positive correlation between As and W and the absence of correlation between Au, Bi, Sb and S.

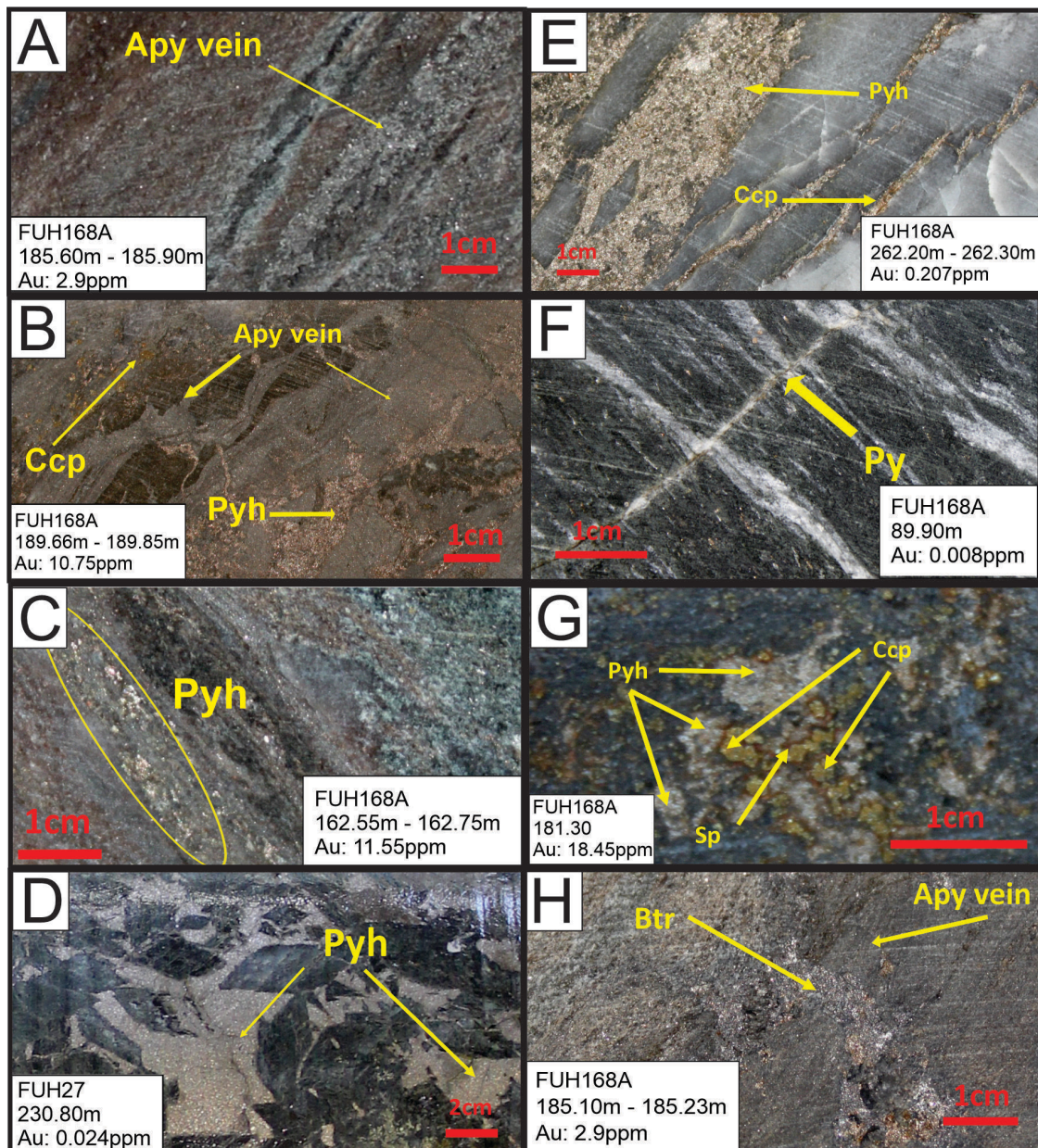


FIGURE 6. (A) Arsenopyrite (Apy) veins parallel to the main foliation and associated with biotite alteration. (B) Arsenopyrite veins associated with Pyrrhotite (Pyh) and Chalcopyrite (Cpy). (C) Pyrrhotite (Pyh) parallel to the main foliation. (D) Pyrrhotite (Pyh) crystals occurring at breccia zone. (E) Pyrrhotite (Pyh) and chalcopyrite (Cpy) occurring as massive sulfide level within quartz vein. (F) Pyrite (Py) filling fracture and within quartz-carbonate vein. (G) Pyrrhotite (Pyh) with associated chalcopyrite (Cpy) and sphalerite (Sph). (H) Berthierite (Bth) associated with arsenopyrite (Apy) vein.

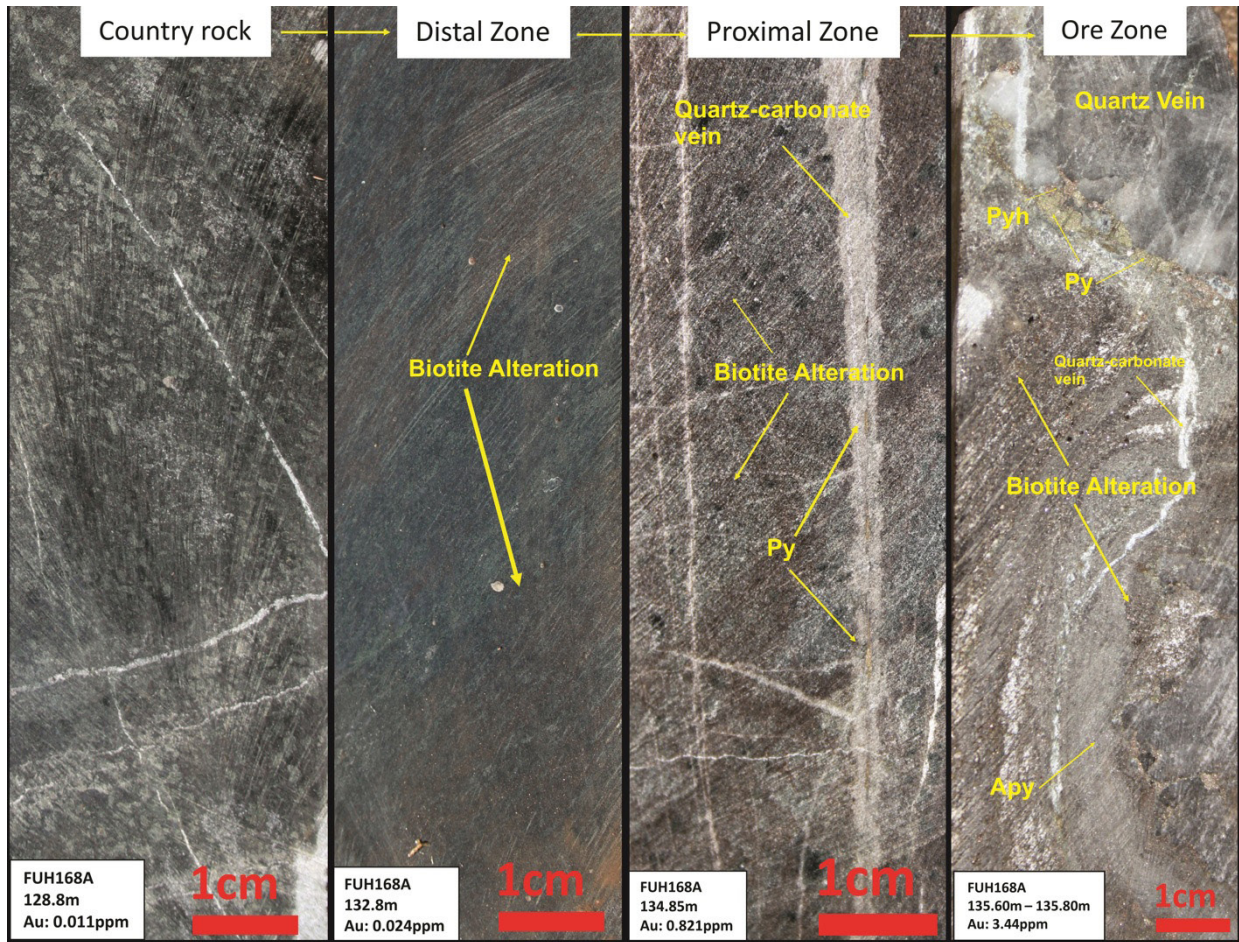


FIGURE 7. Transition from barren host rock to the main ore zone.

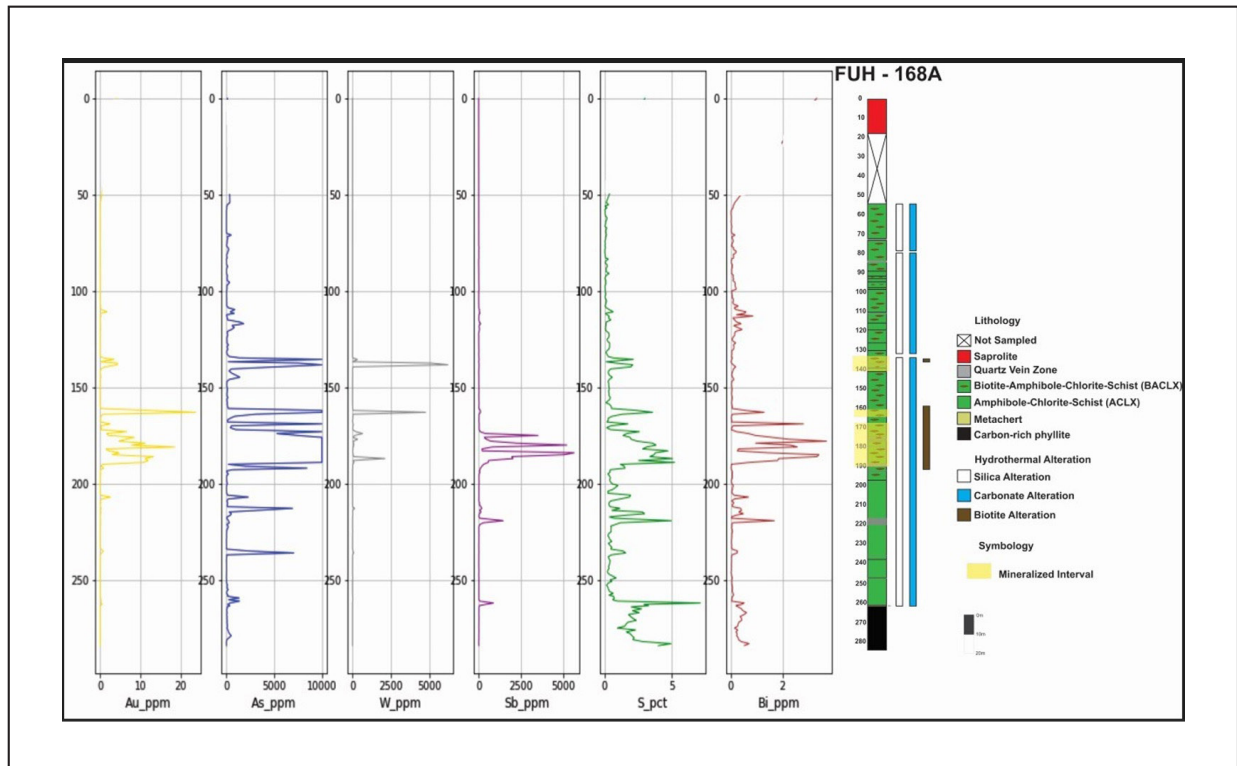


FIGURE 8. FUH168A drill core description and downhole graph for Au, As, W, Sb, S and Bi.

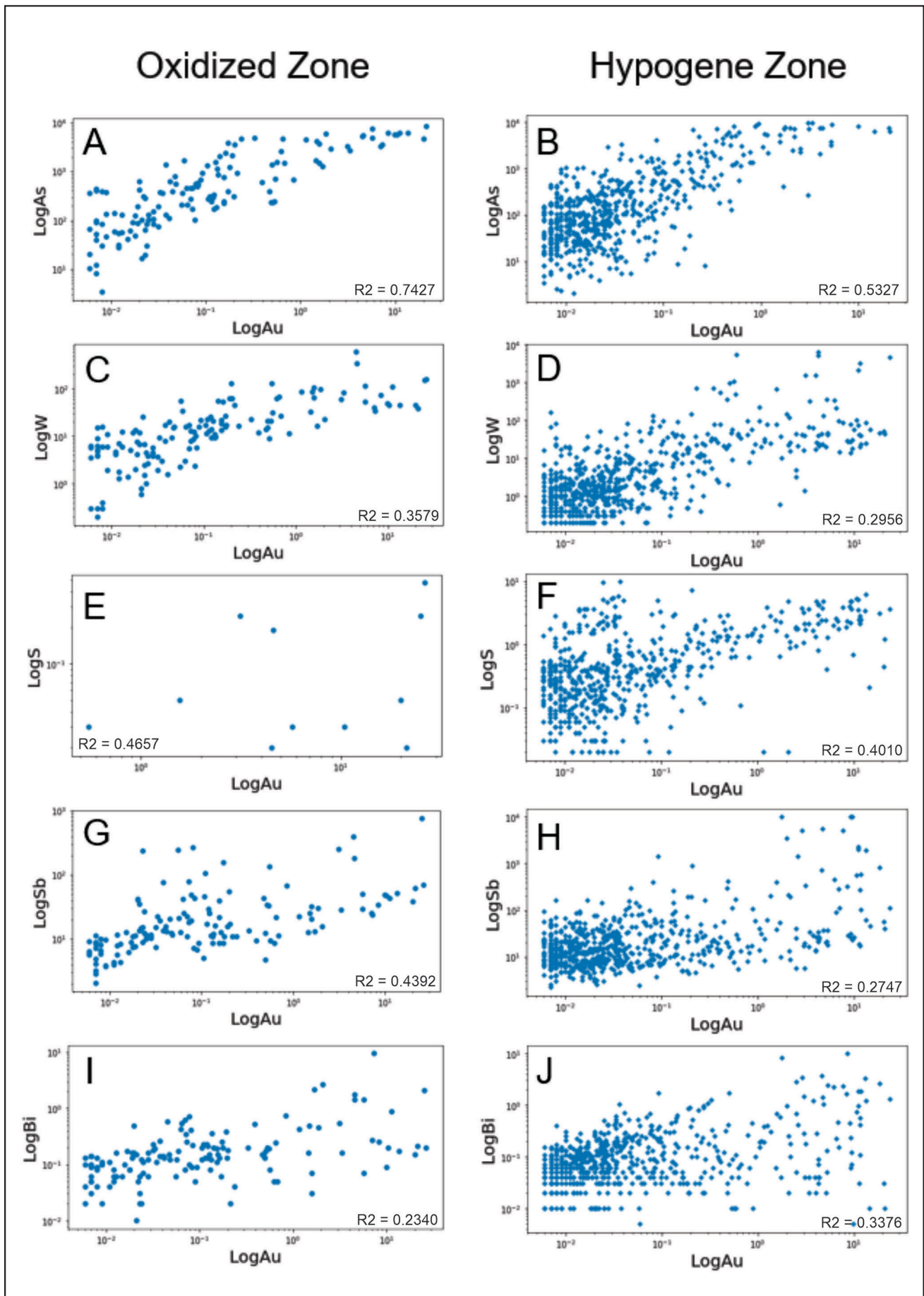


FIGURE 9. Biplot diagrams. (A) and (B) Au x As. (C) and (D) Au x W. (E) and (F) Au x S. (G) and (H) Au x Sb. (I) and (J) Au x Bi.

#### 4.5.1. Multivariate Statistic Methods

Principal component analysis (PCA) for the hypogene zone shows a strong positive covariance between gold, As and W. On the other hand, a negative covariance is observed between gold and Ag, Bi, Mo, Pb, Te, Cu, Zn, Co, Cr and Ni. No covariance is observed between gold and S, Tl and Sb (Figure 10A). The proximity between vectors in the diagram enables the establishment of element associations. The correlation values between elements obtained by the PCA method can also be verified in Table 1. The closer the value is to 1, the stronger the positive correlation, meaning that the concentrations of positively correlated elements increase together. The closer it is to -1, the stronger the negative correlation, meaning that as the concentration of one element increases, the concentration of the other correlated element tends to decrease. Therefore, based on PCA technique and binary plot diagrams, mineralization in the hypogene portion of the Faina deposit displays a geochemical signature of Au-As-W.

PCA for the oxidized portion of Faina deposit shows principal component diagram a strong positive covariance between gold, As and W; a negative covariance is observed between gold, Tl, Te, Cr, Cu, Ni, Zn, Co. At last, no covariance is observed between gold and S, Sb, Ag, Mo, Bi and Pb (Figure 10B). The proximity between vectors in the diagram allows the establishment of element associations. The correlation values between elements obtained by PCA method can also be verified on Table 1. Therefore, based on PCA technique and biplot diagrams, mineralization at oxidized portion of Faina deposit displays a geochemical signature of Au-As-W.

#### 4.6. Major mineralogy by X-ray diffraction (XRD) and Rietveld method

##### 4.6.1. Hypogene Zone

The mineral composition of actinolite-chlorite-schist, estimated through the Rietveld method can be observed in Figure 11. The chart includes results from both mineralized and non-mineralized intervals.

The samples are composed mainly of quartz, plagioclase, amphiboles, chlorite, epidote, prehnite, pumpellyite, and

**TABLE 1:** Correlation table between gold and other elements obtained by principal component analyses.

Element	Hypogene Zone	Oxidized Zone
	Correlation with Au	Correlation with Au
Ag	-0.21	-0.08503
As	0.59	0.7347
Bi	-0.16	0.08291
Cu	-0.47	-0.3586
Mo	-0.52	-0.4906
Pb	-0.43	-0.4692
S	0.039	-0.05497
Sb	-0.053	0.153
Te	-0.56	-0.5978
Tl	-0.0061	-0.5495
W	0.5	0.5798
Zn	-0.55	-0.3661
Ni	-0.57	-0.5164
Cr	-0.48	-0.3501
Co	-0.51	-0.689

10Å phyllosilicates (which corresponds to illite, biotite and muscovite). Arsenopyrite, scheelite, berthierite, native antimony and tetrahedrite were detected only in the mineralized samples.

##### 4.6.2. Oxidized Zone

Based on mineral associations, samples from oxidized zones were divided in two groups: Group 1 and Group 2, which are reported in Figures 12.

Samples from Group 1 are composed mainly of quartz, goethite and 7Å phyllosilicates (which corresponds to kaolinite and halloysite). Minor amounts of relict minerals such as plagioclase, epidote, chlorite, amphiboles, 10Å phyllosilicates, titanite, ilmenite, rutile, calcite, apatite, tourmaline and other alteration minerals including gibbsite, scorodite (0.5%-2.2%,  $\text{FeAsO}_4 \cdot 2\text{H}_2\text{O}$  – alteration product of arsenopyrite), anatase,  $\text{TiO}_2$  – alteration product of titanium rich minerals) and geigerite ( $\text{Mn}_5(\text{AsO}_3\text{OH})_2(\text{AsO}_4)_2 \cdot 10(\text{H}_2\text{O})$ ).

Group 2 samples are composed mainly of quartz, goethite and 7Å phyllosilicates. When compared to samples from Group 1, Group 2 samples present higher proportions of plagioclase, chlorite, amphiboles, 10Å phyllosilicates.

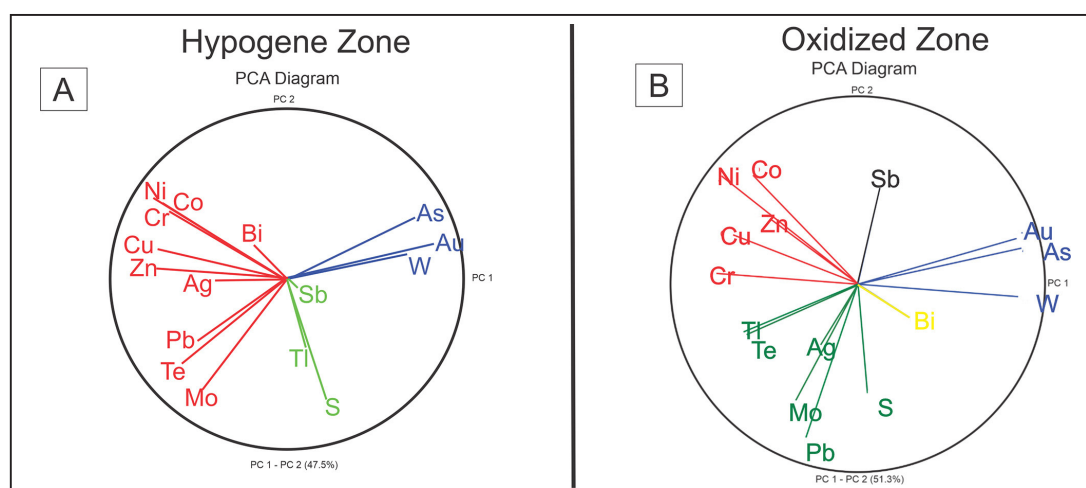


**FIGURE 10.** (A) PCA diagram for the hypogene zone. (B) PCA diagram for the oxidized zone of Faina deposit. Colors were used to highlight different element associations in each diagram.

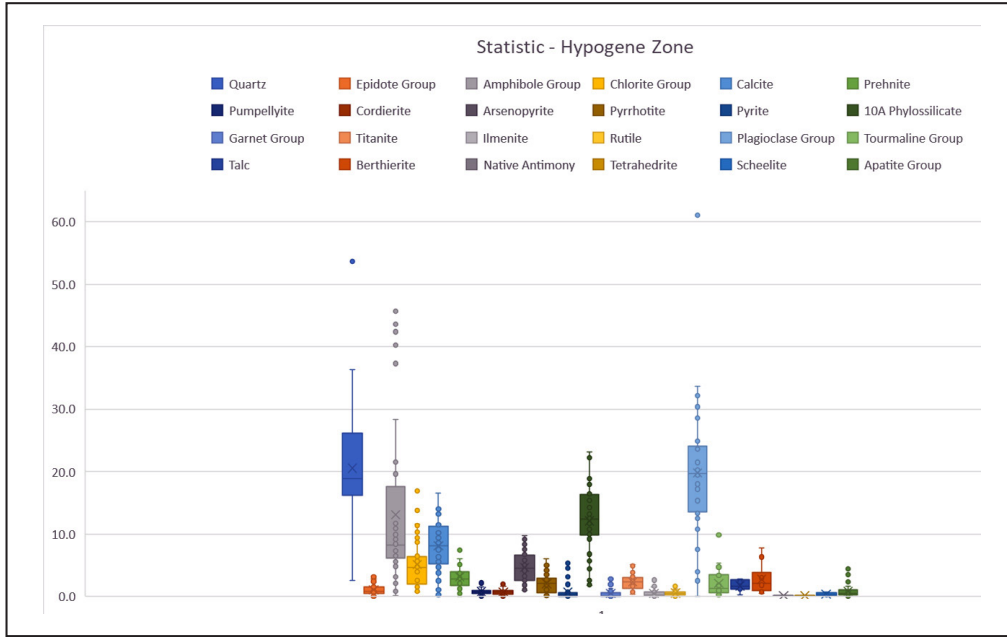


FIGURE 11. Major mineralogy of samples from actinolite-chlorite-schist obtained by XRD. Results includes samples from both mineralized and non-mineralized interval.

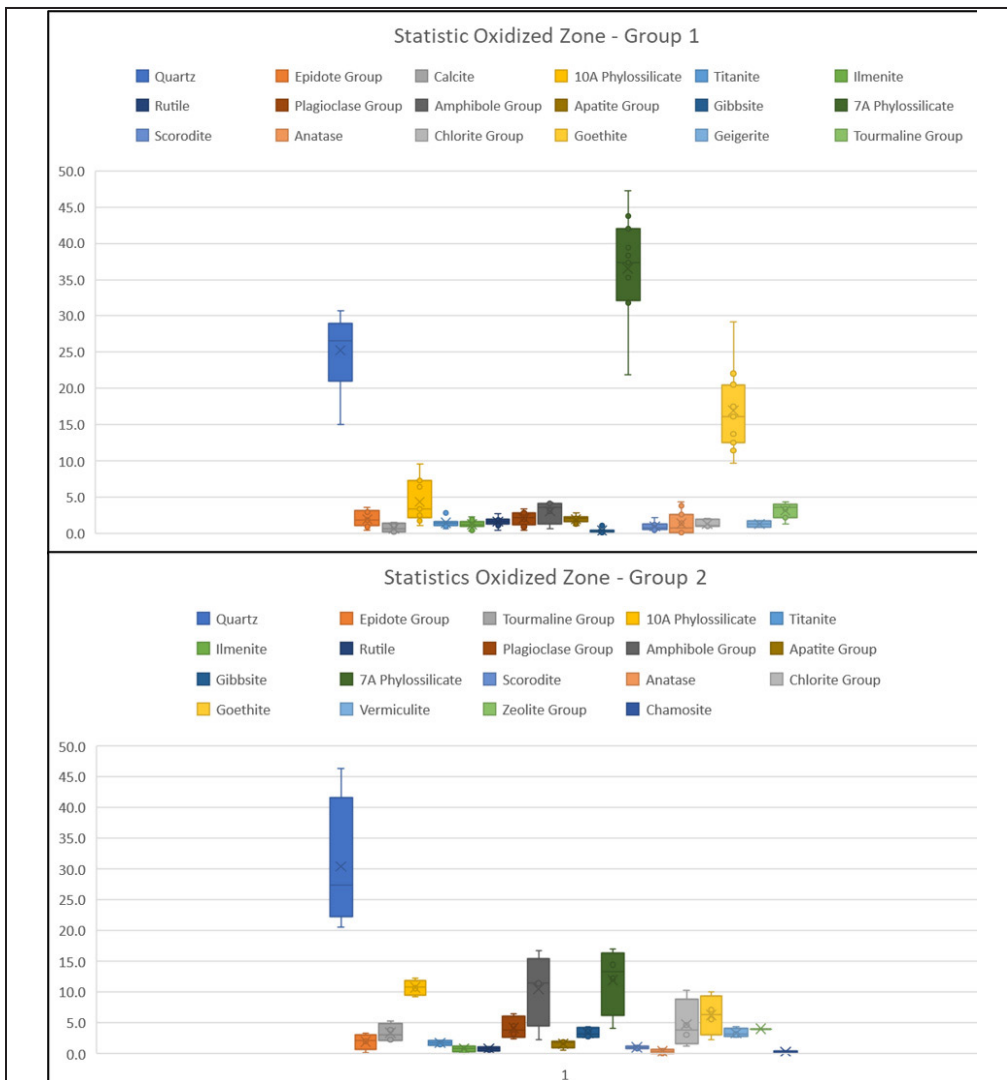


FIGURE 12. Major mineralogy of samples from oxidized zone.

Similar proportions of other minerals such as epidote, titanite, ilmenite, rutile, apatite and tourmaline are still preserved from weathering. In addition, minerals generated by weathering include gibbsite, scorodite, anatase, zeolite group mineral, vermiculite ( $Mg_{1.8}Fe_{0.9}Al_{4.3}SiO_{10}(OH)_{2.4}(H_2O)$ ) and chamosite ( $Fe_3Mg_{1.5}AlFe_{0.5}Si_3AlO_{12}(OH)_6$ ).

#### 4.7. Mineralogy

The opaque minerals identified by reflected-light microscopy were divided in two groups: a) syn-tectonic phases including arsenopyrite, pyrrhotite, ilmenite and rutile, which exhibit a preferred orientation, parallel to the main foliation of the rock; and b) post-tectonic phases which include arsenopyrite, pyrite, pyrrhotite, chalcopyrite, berthierite and gold and are randomly oriented.

**Arsenopyrite:** syn-tectonic arsenopyrite occurs as prismatic and elongated crystals, parallel to the main foliation (Figure 13 A, B and C). Post-tectonic arsenopyrite forms agglomerates disseminated in silicates (Figure 13E) or replacing pyrrhotite (Figure 13F and I).

**Ilmenite:** overgrows arsenopyrite and is associated with rutile as oriented prismatic crystals following the main foliation (Figure 13A and B).

**Rutile:** occurs as inclusions within ilmenite or overgrows arsenopyrite crystals. In this case, it is parallel to the main foliation (Figure 13B).

**Pyrrhotite:** syn-tectonic pyrrhotite occur along to the main foliation (Figure 13D). Post-tectonic pyrrhotite has no preferred orientation, and is frequently replaced by post-tectonic arsenopyrite (Figure 13F and I). Syn-tectonic pyrrhotite may be partially replaced by post-tectonic chalcopyrite and arsenopyrite (Figure 13D). Post-tectonic pyrrhotite also contains inclusions of pyrite (Figure 13H) and can be overgrown by berthierite and chalcopyrite (Figure 13 G and I).

**Pyrite:** occurs as crystals included in pyrrhotite or as crystals close to or overgrowing pyrrhotite (Figure 13G), disseminated in silicates. Pyrite can also occur in association with arsenopyrite (Figure 13I).

**Chalcopyrite:** commonly occurs at the borders of pyrrhotite crystals as replacements (Figure 13D and I)

**Berthierite:** occurs as anhedral crystals, overgrowing pyrrhotite (Figure 13G and I).

**Gold:** occurs as fine anhedral grains at the borders of rutile (Figure 14 A, B and C), as disseminations within silicates, close to arsenopyrite crystals (Figure 14D) or filling fractures (Figure 14E).

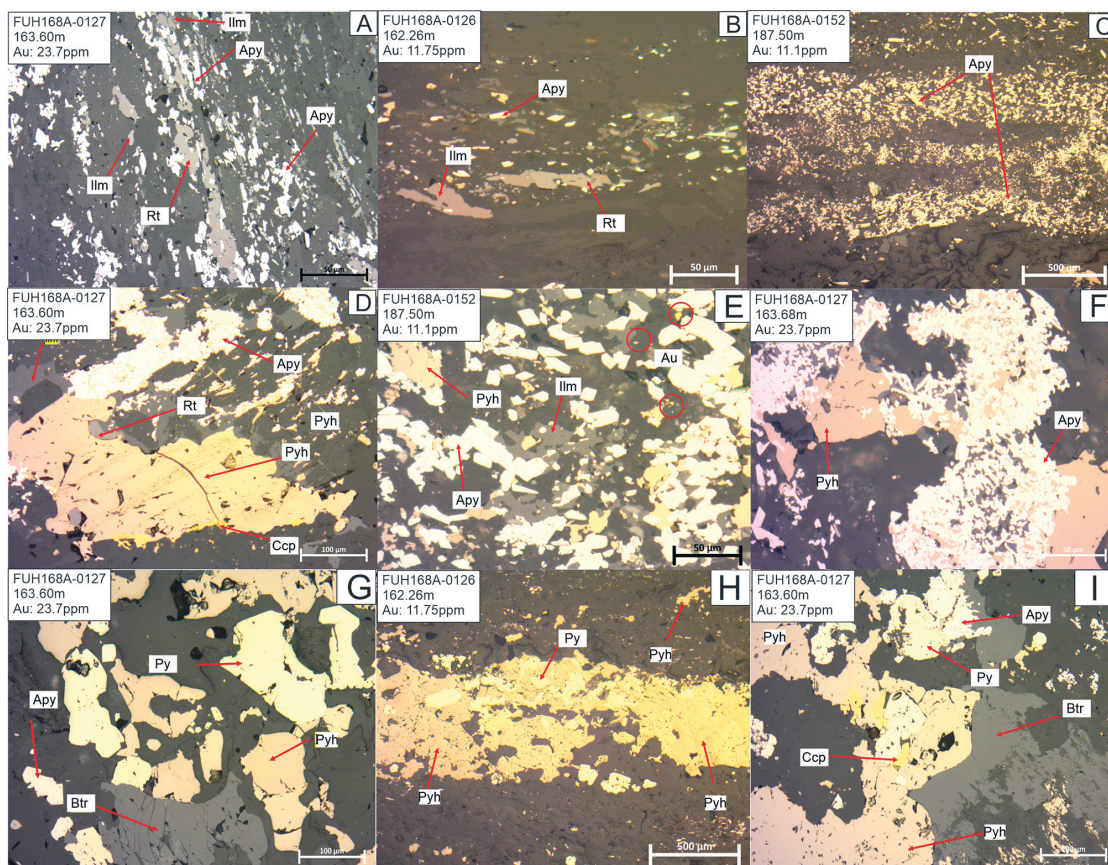


**FIGURE 13.** Photomicrograph of polished sections from mineralized intervals using reflected light microscope, cross polarizers. (A) Syn-tectonic arsenopyrite (Apy) with ilmenite (Ilm) overgrowth. (B) Associated syn-tectonic arsenopyrite (Apy) and ilmenite (Ilm) and rutile (Rt). (C) Syn-tectonic arsenopyrite (Apy) levels parallel to the main foliation. (D) Arsenopyrite (Apy) replacing syn-tectonic pyrrhotite (Pyh). (E) Post-tectonic arsenopyrite (Apy) associated with pyrite (Py) and Ilmenite (Ilm). (F) Post-tectonic arsenopyrite (Apy) replacing post-tectonic Pyrrhotite (Pyh). (G) Associated arsenopyrite (Apy), Pyrite (Py), Pyrrhotite (Pyh) and Berthierite (Bth). (H) Pyrite (Py) inclusions within pyrrhotite (Pyh). (I) Pyrrhotite (Pyh) being replaced by chalcopyrite (Ccp) and with overgrowth of berthierite (Bth).

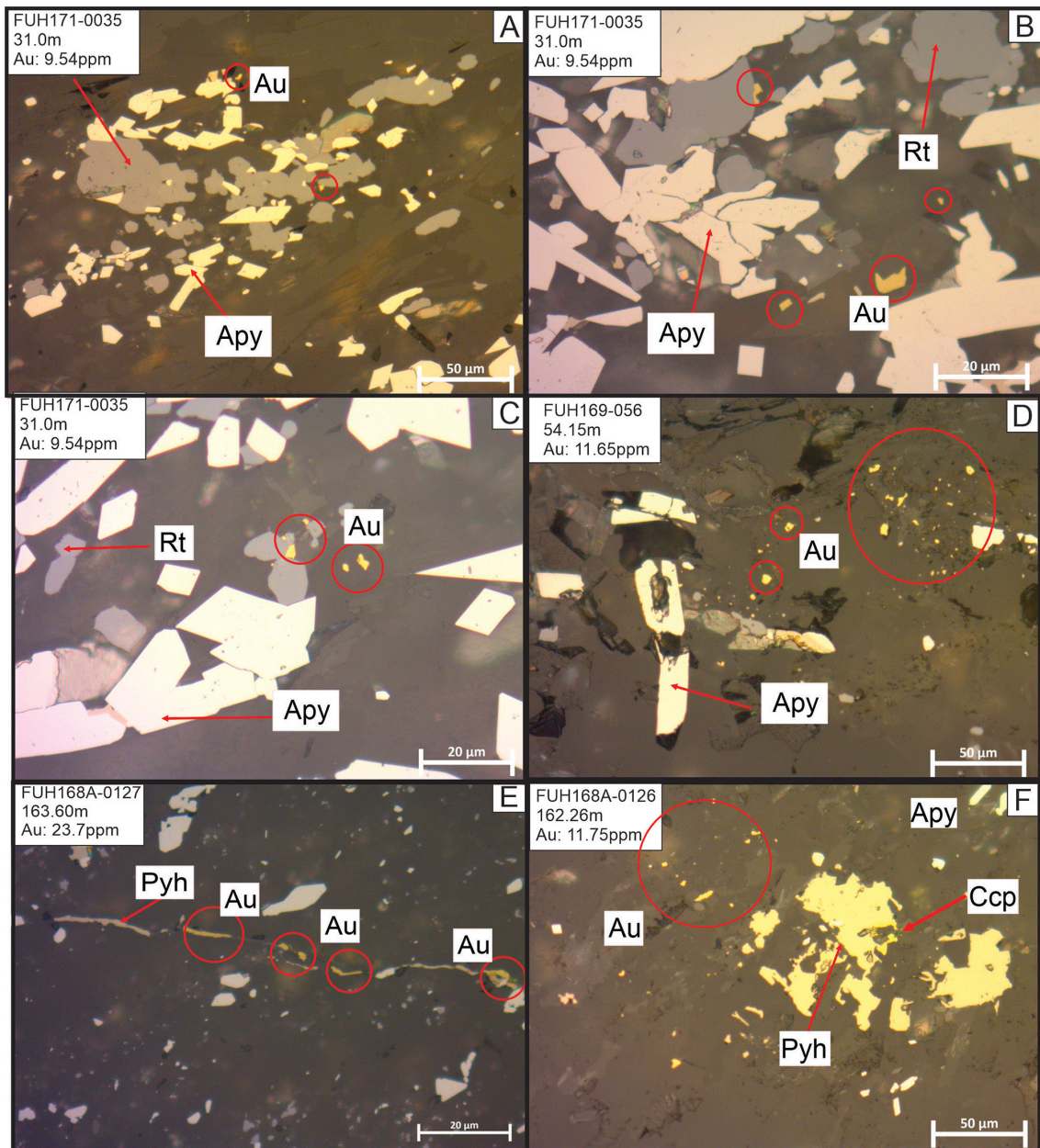


**FIGURE 14.** Photomicrograph of gold particles using reflected light microscope, cross polarizers. (A), (B) and (C) Gold at the borders of rutile (Rt), close to arsenopyrite (Apy). (D) Gold disseminated among silicates, close to arsenopyrite (Apy). (E) Gold filling fracture. (F) Gold disseminated among silicates, close to arsenopyrite (Apy) and post-tectonic pyrrhotite (Pyh).

Backscattered electron images shows that euhedral crystals of arsenopyrite occur as inclusions in pyrrhotite (Figure 15A) or pyrite (Figure 15B and 15C),

Gold occurs as an alloy with silver. Gold is present as inclusions within pyrite (Figure 15C) or at the contact between pyrite and inclusions of arsenopyrite.

Gold also occurs as inclusions within arsenopyrite and pyrrhotite (Figure 16A and B).

Au-Ag alloy was also observed at the borders of arsenopyrite crystals. (Figure 17A, B, C, E and F) and in contact between mica and alkaline feldspar (Figure 17D).

The minerals oriented according to the main foliation of the rock such as arsenopyrite, pyrrhotite, ilmenite and rutile suggest that these minerals were formed during the main deformational event Dn. Arsenopyrite inclusions in pyrrhotite

and pyrite suggest that arsenopyrite replaced these two sulfides. Non-oriented arsenopyrite aggregates overgrowing pyrrhotite provide evidence of a second generation of arsenopyrite, unaffected by deformation. The intergrowths of post-tectonic pyrrhotite and pyrite and between chalcopyrite and pyrite indicate simultaneous crystallization of those sulfides. The occurrence of berthierite overgrowing post-tectonic pyrrhotite is interpreted as the last stage of sulfide generation. Gold was observed at the borders of syn-tectonic sulfides and oxides, as inclusions within sulfides or disseminated among silicates.

Figure 18 illustrates the proposed sequence of crystallization of sulfides and oxides and their correlation with gold mineralization based on textural relationships and mineral associations.

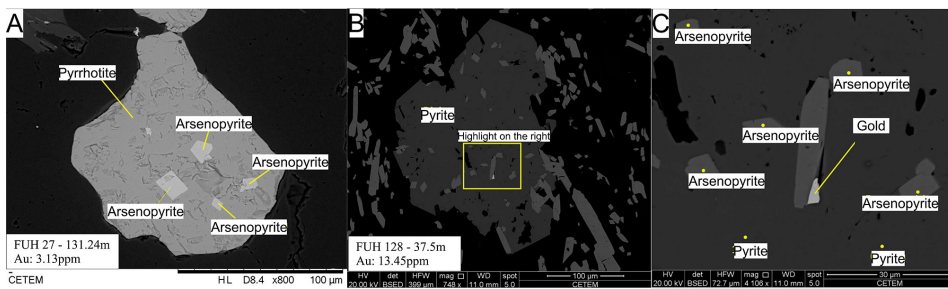


FIGURE 15. (A) Arsenopyrite as inclusions within pyrrhotite. (B) Arsenopyrite as inclusions within pyrite, in contact with pyrite and associated but not included with pyrite. Yellow rectangle is Fig. 16C. (C) Gold as inclusions in pyrite.

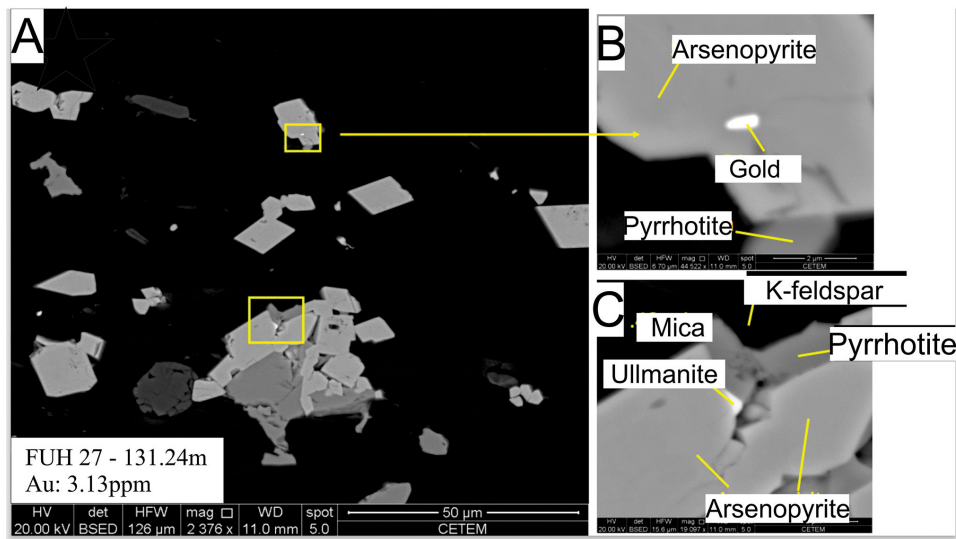


FIGURE 16. (A), (B) and (C) Gold as inclusions within arsenopyrite. Yellow rectangles represent Fig. 11B and 11C.

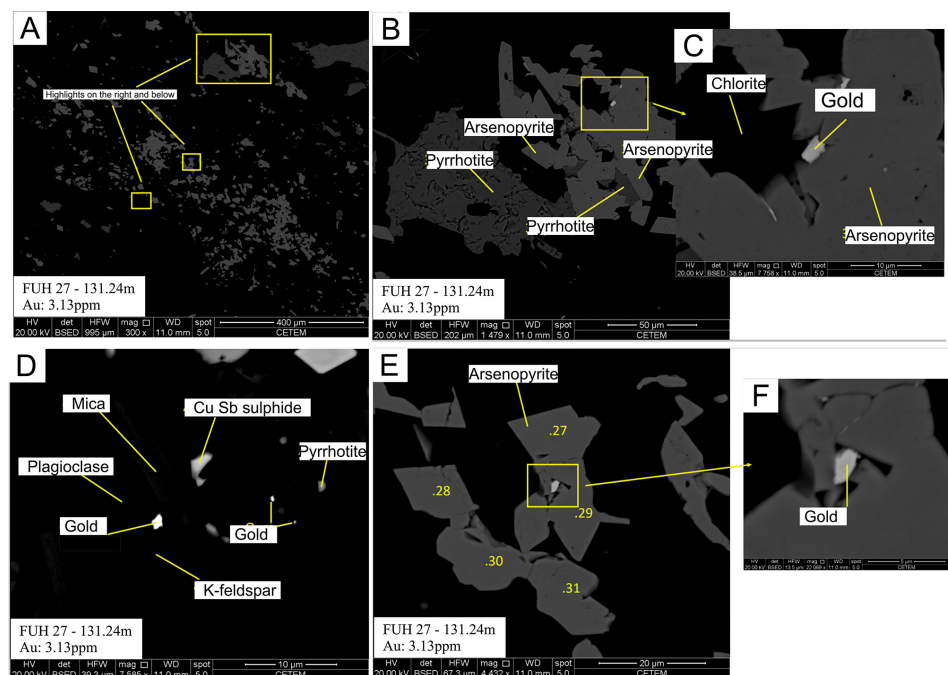


FIGURE 17. (A), (B), (C) Au-Ag alloy at the border of arsenopyrite crystals. (D) Gold in contact with k-feldspar and mica. (E) and (F) Gold at the border of arsenopyrite crystals.

Mineral Phase	Syn-Tectonic	Post-Tectonic
Arsenopyrite	-----	-----
Ilmenite	-----	
Rutile	-----	
Pyrrhotite	-----	
Pyrite		-----
Berthierite		-----
Au	----- ? ? ? -----	-----

FIGURE 18. Sequence of crystallization and timing of Au mineralization.

## 5. Discussion

### 5.1. Geochemical and mineralogy characteristics of the hypogene zone: implications for refractory gold

Direct leaching results for samples in the hypogene zone yielded gold recoveries below 50%. The hypogene zone is characterized by an Au-As-W geochemical association. Arsenopyrite is restricted to intervals with high gold grades. Antimony (as berthierite and native Sb) anomalies also present spatial overlap with Au anomalies, even though this statistical correlation is not as pronounced as Au-As correlation. The reason for the low correlation between Au and Sb, despite the spatial overlap of the anomalies. However, to understand the impact on ore processing, it is important to recognize the presence of Sb anomalies and mineral phases containing this element in intervals enriched in Au. Arsenopyrite, berthierite and pyrrhotite are minerals commonly associated with low performance recovery at gold deposits. (Komnitsas and Pooley 1989; Vaughan 2004; Chryssoulis and McMullen 2016; Rohner and Millard 2016).

The occurrence of gold as fine-grained inclusions, commonly less than 10  $\mu\text{m}$ , along with the presence of leach-robbing minerals (arsenopyrite, pyrrhotite and berthierite) and cyanicides elements (As and Sb) are considered as the main reasons why the Faina gold ore yielded low recoveries during direct leaching tests. This is similar to those documented for Archean gold deposits in South Africa such as Barberton Mountiland, Murchison Range, Sutherland Range and Klipwal Mine (Swash 1988).

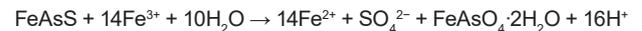
Flotation is highly recommended in cases where gold is associated with leach-robbing sulfides (Bulatovic and Wyslouzil 2000; Peres et al. 2002). The combination of gravimetric concentration and flotation favor reaction of gold with cyanide solution. A new ore processing route, including gravimetric concentration and flotation as concentration methods prior to cyanide leaching, was tested, and the results achieved recoveries higher than 85% (Pressaco et al. 2022). According to Pressaco et al. (2022), the highest recoveries were achieved when 80% of the ore was reduced to a grain size smaller than 53  $\mu\text{m}$ . Backscattered electron images indicate sulfide crystals in Faina ore predominantly have a grain size smaller than 50  $\mu\text{m}$ . During grain size reduction, sulfides crystals hosting gold inclusions are released and exposed to the leaching solution, resulting in higher recoveries. Gravimetric concentration and flotation were essential to concentrate dense sulfide phases

in a smaller volume, further facilitating contact between gold and cyanide solutions.

Due to the lack of mineral chemistry analyses by electron microprobe analysis (EMPA) it is not possible to confirm the amount of gold or even whether gold is chemically locked within sulfide structure (invisible gold). If this is the case, a pre-treatment step such as roasting or bioleaching would be necessary to further increase gold recovery performance. Antimony-bearing ore minerals like berthierite or stibnite require a special treatment during flotation (Bulatovic and Wyslouzil 2000; Rohner and Millard 2016), which involves maintaining the pH around 12, a condition that allows for the controlled reaction of Sb minerals with cyanide (Hedley and Tabachnick 1958; Rohner and Millard 2016).

### 5.2. Geochemical and mineralogical characteristics of oxidized zone: implications for gold recovery

The oxidized section of Faina presents high arsenic grades, with a strong positive correlation to gold. The XRD analysis did not detect any sulfides and geochemical analyses yielded sulfur grades up to 0.47%, which is too low to form sulfide phases. Based on the XRD data, the sulfide phase in the oxidized zone is primarily characterized by scorodite, the main alteration product of arsenopyrite (Murciego et al. 2011; Basu and Schreiber 2013). This phase forms under acidic and oxidizing conditions as shown by the following reaction (Dove and Rimstidt 1985):



Weathering completely converted arsenopyrite to scorodite, while pyrite and pyrrhotite were transformed into iron hydroxides and sulfates (Nicholson and Scharer 1984; Wang et al. 2022). The sulfate remained in solution and was leached, resulting in lower sulfur grades. Gold that was (physically or chemically) locked within sulfides was fully liberated, making it accessible to cyanide ions. As a result, recovery in the oxidized portion was higher than 90% even with direct leaching. The reaction of sulfide alteration and liberation of gold particles is shown in Figure 19.

Bismuth and Sb anomalies exhibit spatial overlap with gold and their presence could potentially reduce gold recovery (Vaughan 2004; Bulatovic and Wyslouzil 2000; Adams 2016). In the oxidized zone, however, Bi and Sb values range, up to 9.46ppm and 751ppm, respectively., which are no high enough to form mineral phases composed of these elements. Therefore, it is unlikely they will not present negative effects during direct leaching.

### 5.3. Comparison between Faina and other auriferous gold deposits

The Faina deposit is a shallow (<50m) and intensely weathered horizon with high-grade gold intervals, primarily composed of quartz, goethite, kaolinite, halloysite and minor amounts of other clay minerals. In these intervals, all the hypogene sulfides have been destroyed and gold initially present as submicroscopic particles within sulfides or tellurides were remobilized and redeposited as native gold. Gold recovery in these oxidized zone ranges between 90% and 95%.

This study is compared with similar studies conducted by Vaughan and Kyin (2004) on several gold deposits located

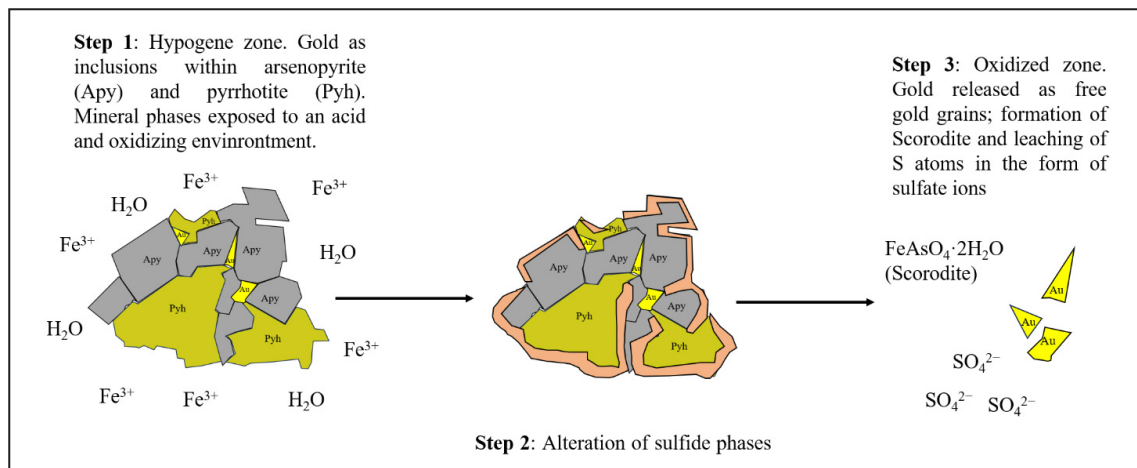


FIGURE 19. Reaction of alteration of sulfide phases on an acid and oxidizing environment releasing gold and forming scorodite.

at Yilgarn Craton in Western Australia, aimed at defining the causes of low recoveries in refractory ores and comparing those characteristics with free-milling ores. In their study, they found that the main reason for low gold recoveries at those deposits was the presence of submicroscopic gold within sulfide crystal structures.

The deposits in the Yilgarn Craton are moderately to deeply weathered yielding thick (up to 100m) oxidized gold deposits. The supergene processes that affected the gold deposits studied by Vaughan and Kyin (2004) can be considered analogous to the oxidized zone of Faina deposit sulfide destruction by weathering processes leads to subsequent gold liberation.

In the non-weathered portion of the Yilgarn gold deposits, the ore is mostly refractory, with gold present as submicroscopic particles within arsenopyrite and pyrite structures. However, a portion of the gold mineralization associated with sulfides (arsenopyrite and pyrite) occurs as free-milling gold. This portion underwent recrystallization during structural evolution and burial in the crust, causing the gold to be expelled from the sulfide structure and re-deposited as native gold along arsenopyrite microfractures, at the borders of sulfide crystals, or among gangue minerals (Vaughan and Kyin 2004)

Simmard et al. (2013) proposed a similar evolution in their research on the Lapa gold mine in the Abitibi subprovince. This deposit also exhibits low recoveries and shares several similarities with Faina such as meta-mafic rocks as host unit, clear association between gold mineralization and sulfides (mainly arsenopyrite), biotite alteration, and the presence of As and Sb. Gold in Lapa mine occurs as angular grains inclusions in arsenopyrite aggregates, along pyrrhotite and arsenopyrite margins or as free-milling gold among silicates. Gold locked within the sulfide structure is a key factor contributing to low recovery rates. However, gold occurring as free grains was liberated due to the progressive metamorphism and recrystallization of arsenopyrite. In the Faina deposit, gold is present not only as inclusions, but also as free grains. It is interpreted that processes similar to those described above occurred at Faina d, as part of the gold is locked as inclusions while another portion is present as free grains, which were released as a consequence of arsenopyrite recrystallization during an increase in temperature.

In another study by Brando Soares et al. (2018) on the São Sebastião deposit, located about 22km to the east of Faina deposit, and also hosted within rocks from the Pitangui greenstone belt (Figure.1), a similar link between recrystallization and non-refractory arsenopyrite- and pyrrhotite bearing ores was established). The São Sebastião ore also contains an Au-Bi-As association (but not W-Au). At São Sebastião deposit, post-depositional heating triggered gold scavenging by Bi, which consequently improved gold recovery. At Faina deposit, gold occurs within more deformed and recrystallized sulfides when compared to São Sebastião deposit, but with a similar chemical association. Despite these similarities between the Faina and São Sebastião deposits, no evidence was found for gold scavenging by Bi. However, more recent work has shown evidence for gold scavenging by Sb at the hinge zone of the Faina deposit (Gonçalves et al. 2023; Silveira et al. 2023).

## 6. Conclusions

The stratigraphy at Faina consists of a hypogene zone dominated by sulfide-rich meta-mafic rocks and meta-sedimentary rocks, overlain by an oxidized, weathered horizon. Economic gold mineralizations is hosted within both the hypogene and oxidized zones. Distinct geological evolutionary histories have created contrasting mineralogical and geochemical associations. In the hypogene zone, the geochemical signature is characterized by Au-As-W, with mineralization strongly associated with multiple hydrothermal alterations such as quartz-carbonate veins, biotite alteration and sulfidation. Gold occur as free-milling particles, and as inclusions within sulfides. On the other hand, in the oxidized zone, the geochemical signature includes Au-As-W-Sb, with gold with arsenates, quartz, iron-hydroxides and clay minerals.

Geochemical and mineralogical differences directly influence gold recoveries necessitating different processing flowcharts. Submicroscopic gold physically "locked" within sulfides is less available to react with leaching solution and therefore requires finer grain-size reduction. Moreover, the presence of leach-robbing minerals decreases the availability of cyanide ions to dissolve gold, consequently reducing efficiency. In contrast to similar deposits in the Pitangui

greenstone belt, such as São Sebastião, gold has probably undergone scavenging by Sb and not Bi in specific portions of the deposit. In the oxidized zone, however, the sulfides have been completely altered by weathering, resulting in the release of gold, which is now accessible to cyanide ions.

The results of this research emphasize the importance of a multi-methodological approach and a detailed characterization of gold ores. A couple, d precise, and thorough petrographic and geochemical investigation can be one of the key factors contributing to successful decision-making during mineral exploration and mining programs. Understanding the textures, morphologies and chemistry of gold ores, as well as their links with evolutionary processes may lead to better recovery control and refined ore processing flowcharts.

## Acknowledgements

The authors thank Jaguar Mining Inc., for providing samples, multi-element analyses, geological data and for all logistical and financial support that make the research possible. The authors also thank Centre for Mineral Technology (CETEM) for SEM and XRD facilities and Laboratory of Petrology (UERJ) for the optical microscopy facilities.

## Editor acknowledgement

The Editor-in-Chief acknowledges the contribution of Napoleon Hammond and one anonymous reviewer.

## Authorship credits

Author	A	B	C	D	E	F
GMS						
AVCN						
MBS						
FEAA						
NOFS						
PABS						
VDS						
GFG						

**A** - Study design/ Conceptualization **B** - Investigation/ Data acquisition  
**C** - Data Interpretation/ Validation **D** - Writing  
**E** - Review/Editing **F** - Supervision/Project administration

## References

- Adams M.D. 2016. Gold ore processing: project development and operations. 2nd ed. USA, Elsevier Science, 1020 p.
- Aitchison J. 1986. The statistical analysis of compositional data. New York, Chapman and Hall, 416.
- Alkmim F.F., Marshak S. 1998. Transamazonian orogeny in the Southern São Francisco craton region, Minas Gerais, Brazil: evidence for Paleoproterozoic collision and collapse in the Quadrilátero Ferrífero. *Precambrian Research*, 90, 29-58. [https://doi.org/10.1016/S0301-9268\(98\)00032-1](https://doi.org/10.1016/S0301-9268(98)00032-1)
- Alkmim F.F., Teixeira W. 2017. The Paleoproterozoic Mineiro Belt and the Quadrilátero Ferrífero. In: Heilbron M., Cordani U., Alkmim F. (eds). São Francisco Craton, Eastern Brazil. *Regional Geology Reviews*. Springer, p. 71-94. [https://doi.org/10.1007/978-3-319-01715-0\\_5](https://doi.org/10.1007/978-3-319-01715-0_5)
- Alves F.E.A., Corrêa Neto A.V., Brando Soares M., Neumann R., Silva G.M., Silva G.P., Varca A.C., Sampaio P.A.B., Silveira V.D. 2022. Genetic implications from textures, mineralogy, and geochemistry: the case of Zona Basal – a singular polymetallic occurrence in the Quadrilátero Ferrífero, Brazil. *Contributions to Mineralogy and Petrology*, 177(48). <https://doi.org/10.1007/s00410-022-01913-w>
- Baltazar O.F., Lobato L.M. 2020. Structural evolution of the Rio das Velhas Greenstone Belt, Quadrilátero Ferrífero, Brazil: influence of Proterozoic Orogenies on Its Western Archean Gold Deposits. *Minerals*, 10(11), 983. <https://doi.org/10.3390/min10110983>
- Baltazar O.F., Zucchetti M. 2007. Lithofacies associations and structural evolution of the Archean Rio das Velhas greenstone belt, Quadrilátero Ferrífero, Brazil: A review of the setting of gold deposits. *Ore Geology Reviews*, 32(3-4), 471-499. <https://doi.org/10.1016/j.oregeorev.2005.03.021>
- Basu A., Schreiber M.E. 2013. Arsenic from arsenopyrite weathering: Insights from sequential extraction and microscopic studies. *Journal of Hazardous Materials*, 262, 896-904. <https://doi.org/10.1016/j.jhazmat.2012.12.027>
- Brando Soares M., Corrêa Neto A.V., Zeh A., Cabral A.R., Pereira L.F., Prado M.G.B., Almeida A.M., Manduca L.G., Silva P.H.M.; Mabub, R.O.A.; Schlichta, T.M. 2017. Geology of the Pitangui greenstone belt, Minas Gerais, Brazil: Stratigraphy, geochronology and BIF geochemistry. *Precambrian Research*, 291, 17-41. <https://doi.org/10.1016/j.precamres.2017.01.008>
- Brando Soares M., Corrêa Neto A.V., Bertolino L.C., Alves F.E.A., Almeida A.M., Siva P.H.M., Mabub R.O.A., Manduca L.G., Araújo I.M.C.P. 2018. Multistage mineralization at the hypozonal São Sebastião gold deposit Pitangui greenstone belt, Minas Gerais, Brazil. *Ore Geology Reviews*, 102, 618-638. <https://doi.org/10.1016/j.oregeorev.2018.09.028>
- Bruno H., Elizeu V., Heilbron M., Valeriano C.M., Strachan R., Fowler M., Bersan S., Moreira H., Dussin I., Silva L.G.E., Tupinambá M.; Almeida J., Neto C., Storey C. 2020. Neoproterozoic and Rhyacian TTG-sanukitoid suites in the southern São Francisco Paleoproterozoic, Brazil: Evidence for diachronous change towards modern tectonics. *Geoscience Frontiers*, 11, 1763-1787. <https://doi.org/10.1016/j.gsf.2020.01.015>
- Bruno H., Heilbron M., Valeriano C.M., Strachan R., Fowler M., Bersan S., Moreira H., Motta R., Almeida J., Almeida R.; Carvalho M., Storey C. 2021. Evidence for a complex accretionary history preceding the amalgamation of Columbia: The Rhyacian Minas Bahia Orogen, southern São Francisco Paleoproterozoic, Brazil. *Gondwana Research*, 92, 149-171. <https://doi.org/10.1016/j.gr.2020.12.019>
- Buccianti A., Mateu-Figueras G., Pawlowsky-Glahn V. (eds.). 2008. Compositional data analysis in the geosciences: from theory to practice. *Stoch Environ Res Risk Assess*, 22, 139-141. <https://doi.org/10.1007/s00477-007-0193-3>
- Bulatovic S., Wyslouzil D.M. 2000. Gold recovery: flotation. In: Wilson I.D. (ed.). *Encyclopedia of Separation Science*. Academic Press. 2965-2975. <https://doi.org/10.1016/B0-12-226770-2/05871-3>
- Carneiro M.P. 1992. O Complexo metamórfico Bonfim setentrional (Quadrilátero Ferrífero, MG): litoestratigrafia e evolução geológica de um segmento de crosta continental do Arqueano. PhD Thesis, Universidade de São Paulo. <https://doi.org/10.11606/T.44.1992.tde-18112015-104751>
- Cheary R.W., Coelho A. 1992. Fundamental parameters approach to X-ray line-profile fitting. *Journal of Applied Crystallography*, 25, 109-121. <https://doi.org/10.1107/S0021889891010804>
- Chrystouli S.L., McMullen J. 2016. Mineralogical investigation of gold ores. *Developments In Mineral Processing*, 15, 21-71. [https://doi.org/10.1016/S0167-4528\(05\)15002-9](https://doi.org/10.1016/S0167-4528(05)15002-9)
- Costa F.R., Nery G.P., Carneiro C.C., Kahn H., Ulsen C. 2022. Mineral characterization of low-grade gold ore to support geometallurgy. *Journal of Material, Research and Technology*, 21, 2841-2852. <https://doi.org/10.1016/j.jmrt.2022.10.085>
- Dorr J.V.N. 1969. Physiographic, stratigraphic, and structural development of the Quadrilátero Ferrífero, Minas Gerais, Brazil. Washington, US Government Printing Office, p. 110. (Geological Survey professional paper; 641-A).
- Dove P.M., Rimstidt J.A. 1985. The solubility and stability of scorodite, FeAsO<sub>4</sub>.2H<sub>2</sub>O, *American Mineralogist*, 70, 838-844. Available online at: <https://pubs.geoscienceworld.org/msa/ammin/article-abstract/70/7-8/838/41779/The-solubility-and-stability-of-scorodite-FeAsO4?redirectedFrom=fulltext> / (accessed on 13 June 2025).
- Egozcue J.J., Pawlowsky-Glahn V., Mateu-Figueras G., Barcelo-Vidal C. 2003. Isometric logratio transformations for compositional data analysis. *Mathematical Geology*, 35, 279-300. <https://doi.org/10.1023/A:1023818214614>
- Fabricio-Silva W., Rosiere C.A., Buhn B. 2018. The shear zone-related gold mineralization at the Turmalina deposit, Quadrilátero Ferrífero, Brazil: structural evolution and the two stages of mineralization. *Mineralium Deposita*, 54, 347-368. <https://doi.org/10.1007/s00126-018-0811-7>

- Feng D., Van Deventer J. 2010. Effect of thiosulphate salts on ammoniacal thiosulphate leaching of gold. *Hydrometallurgy*, 105, 120–126. <https://doi.org/10.1016/j.hydromet.2010.08.011>
- Goldfarb R.J., Groves D.I. 2015. Orogenic gold: common or evolving fluid and metal sources through time. *Lithos*, 233, 2-26. <https://doi.org/10.1016/j.lithos.2015.07.011>
- Gonçalves G.F., Silveira V.D., Corrêa Neto A.V., Brando Soares M., Souza M.O.A., Massucatto A.J. 2023. Mineralização aurífera complexa em estruturas arqueanas reativadas: Estudo de caso do Greenstone Belt Pitangui, MG. In: Simpósio Brasileiro de Metalogenia, 5, 85. Available online at: [www.ufrgs.br/sbm2023/sites/default/files/anexospagina/anais-v-sbm-2023.pdf](http://www.ufrgs.br/sbm2023/sites/default/files/anexospagina/anais-v-sbm-2023.pdf) / (accessed on 7 January 2025)
- Grazulis S., Chateigner D., Downs R.T., Yokochi A.F.T., Quirós M., Lutterotti L., Manakova, E., Butkus J., Moeck P., Le Bail A., 2009. Crystallography Open Database – an open-access collection of crystal structures. *J. Appl. Crystallogr.* 42, 726–729. <https://doi.org/10.1107/S0021889809016690>
- Groves D.I., Goldfarb R.J., Gebre-Mariam M., Hagemann S.G., Robert F. 1998. Orogenic gold deposits: a proposed classification in the context of their crustal distribution and relationship to other gold deposit types. *Ore Geology Reviews*, 13, 7-27. [https://doi.org/10.1016/S0169-1368\(97\)00012-7](https://doi.org/10.1016/S0169-1368(97)00012-7)
- Grunsky E.C. 2010. The interpretation of geochemical survey data. *Geochemistry: Exploration, Environment, Analysis*, 10, 27-74. <https://doi.org/10.1144/1467-7873/09-210>
- Grunsky E.C., Caritat P. 2019. State-of-art analysis of geochemical data for mineral exploration. *Geochemistry: Exploration, Environment, Analysis*, 20, 217-232. <https://doi.org/10.1144/geochem2019-031>
- Hart C. J. R. 2007. Reduced Intrusion-related gold systems. In: Goodfellow W.D. *Mineral Deposits of Canada: a synthesis of major deposit-types district metallogeny, the evolution of geological provinces and exploration methods*. Geological Association of Canada, Mineral Deposits Division, 95-112.
- Hedley N., Tabachnick H. 1958. *Chemistry of cyanidation*. New York, American Cyanamid Company. (Mineral Dressing Notes 23).
- Jaguar Mining. Jaguar Mining reports updated mineral reserves and mineral resources for its MTL Complex including Faina and Pitangui Projects. Published on December 18th 2023. Available online at: <https://jaguarmining.com/files/2024/03/application/65f37296dc7d5.pdf> (accessed on 24 June 2025).
- Komnits C., Pooley F.D. 1989. Mineralogical characteristics and treatment of refractory gold. *Minerals Engineering*, 2(4), 449-457. [https://doi.org/10.1016/0892-6875\(89\)90080-0](https://doi.org/10.1016/0892-6875(89)90080-0)
- Lana C., Alkmim F.F., Armstrong R., Scholz R., Romano R., Nalini H.A. 2013. The ancestry and magmatic evolution of Archaean TTG rocks of the Quadrilátero Ferrífero province, southeast Brazil. *Precambrian Research*, 231, 157–173. <https://doi.org/10.1016/j.precamres.2013.03.008>
- Lang A.M., Aasly K., Ellefmo S.L. 2018. Mineral characterization as a tool in the implementation of geometallurgy into industrial mineral mining. *Mineral Engineering*, 116, 114-122. <https://doi.org/10.1016/j.mineng.2017.10.021>
- Lobato L.M., Ribeiro-Rodrigues L.C., Zucchetti M., Noce C., Baltazar O., Silva L., Pinto C. 2001a. Brazil's premier gold province. Part I: the tectonic, magmatic, and structural setting of the Archaean Rio das Velhas greenstone belt, Quadrilátero Ferrífero. *Mineralium Deposita*, 36(3), 228-248. <https://doi.org/10.1007/s001260100179>
- Lobato L.M., Ribeiro-Rodrigues L.C., Vieira F.W.R. 2001b. Brazil's premier gold province. Part II: geology and genesis of gold deposits in the Archaean Rio das Velhas greenstone belt, Quadrilátero Ferrífero. *Mineralium Deposita*, 36, 249-277. <https://doi.org/10.1007/s001260100180>
- Machado N., Carneiro M.A. 1992. U–Pb evidence of late Archaean tectono-thermal activity in the southern São Francisco shield, Brazil. *Canadian Journal of Earth Sciences*, 29, 2341–2346. <https://doi.org/10.1139/e92-182>
- Mano E.S.; Caner L.; Petit S.; Chaves A.P. 2020. Mineralogical characterization of Copper lateritic ore from Furnas deposit, Carajás, Brazil. *REM – International Engineering Journal*, 73, 329-335. <https://doi.org/10.1590/0370-44672019730113>
- Marinho, M. S.; Silva, M. A.; Lombello, J. C.; Di Salvio, L. P.; Silva, R. N.; Féboli, W. L.; Brito, D. C. 2018. Mapa geológico e de recursos minerais integrado: área de relevante interesse mineral, ARIM, Quadrilátero Ferrífero, faixa Pará de Minas-Pitangui. Belo Horizonte, CPRM. Escala 1:75.000. 1 mapa. Available on line at: <https://rigeo.sgb.gov.br/handle/doc/19393> / (accessed on 7 January 2025)
- Melo-Silva P., Amaral W.S., Oliveira E.P. 2020. Geochronological evolution of the Pitangui greenstone belt, southern São Francisco Craton, Brazil: Constraints from U-Pb zircon age, geochemistry and field relationships. *Journal of South American Earth Sciences*, 99, 102380. <https://doi.org/10.1016/j.jsames.2019.102380>
- Murciego A., Álvarez-Ayuso E., Pellitero E., Rodríguez M.A., García-Sánchez A., Tamayo A., Rubio J., Rubio F., Rubin J. 2011. Study of arsenopyrite weathering products in mine wastes from abandoned tungsten and tin explorations, 186, 590-601. <https://doi.org/10.1016/j.jhazmat.2010.11.033>
- Nicholson R.V., Scharer J.M. 1984. Laboratory studies of pyrrhotite oxidation kinetics. In: Alpers C.N., Blowers D.W. (eds.) *Environmental geochemistry of sulfide oxidation*, Washington, DC, 14-30. (ACS Symposium Series, 550). DOI: [10.1021/bk-1994-0550.ch002](https://doi.org/10.1021/bk-1994-0550.ch002)
- Nude P.M., Asigri J.M., Yidana S.M., Arhin E., Foli G., Kutu J.M. 2012. Identifying Pathfinder elements for gold in multi-element soil geochemical data from the Wa-Lawra Belt, northwest Ghana: a multivariate statistical approach. *International Journal of Geosciences*, 3, 62-70. DOI: [10.4236/ijg.2012.31008](https://doi.org/10.4236/ijg.2012.31008)
- Peres A.E.C., Chaves A.P., Lins F.A.F., Torem M.L. 2002. Beneficiamento de minérios de ouro. In: Trindade R.B.E., Barbosa Filho O. *Extração de ouro: princípios, tecnologia e meio ambiente*. Rio de Janeiro, CETEM/MC, 23-58. cap. 2. Available on line at: <http://mineralis.cetem.gov.br/handle/cetem/687> / (accessed on 7 January 2025)
- Pressaco R.; El-Rassi D.; Lopes R.G.; Landry P.; Blaho S.R.; Sepp J.; Scholey B.J.Y. 2022. *Technical Report on the Turmalina Mine Complex*, Minas Gerais, Brazil. SLR Consulting.
- Ribeiro-Rodrigues L.C.; Oliveira S.M.; Friedrich G. 2007. The Archaean BIF-hosted Cuiabá Gold deposit, Quadrilátero Ferrífero, Minas Gerais, Brazil. *Ore Geology Reviews*, 32(3-4), 543–570. <https://doi.org/10.1016/j.oregeorev.2006.09.001>
- Robb L. 2005. *Introduction to ore-forming processes*. 1<sup>st</sup> ed. Malden-USA, Blackwell Publishing, 373 p.
- Romano A. 2007. *Geologia da folha Pará de Minas SE.23-ZC-IV: escala 1:100.000*. Brasília; Belo Horizonte, CPRM; UFMG, 72 p. Available on line at: <https://rigeo.sgb.gov.br/handle/doc/10765> / (accessed on 7 January 2025)
- Rohner P.; Millard M. 2016. *Treatment of Antimonial Gold Ores*. In: *Book Gold Ore Processing: project development and operations*. 2nd ed. USA, Elsevier, Cambridge, 927-933. <https://doi.org/10.1016/B978-0-444-63658-4.00052-9>
- Silva-Alves G. P.; Corrêa Neto A. V.; Brando Soares M.; Neumann R.; Alves F. E. A.; Souza T. P. 2022. A multi-methodological approach for mineral exploration and predictive metallurgy: the case of the Pilar gold deposit at the Quadrilátero Ferrífero. *Ore Geology Reviews*, 149. <https://doi.org/10.1016/j.oregeorev.2022.105113>
- Silva M.A., Pinto C.P., Pinheiro M.A.P., Marinho M.S., Lombello J.C., Pinho J.M.M.P., Goulart L.E.A., Magalhães J.R. 2020. Mapa geológico do estado de Minas Gerais. Belo Horizonte, CPRM, 2020. 1 mapa. Escala 1:1.000.000. Available online at: <https://rigeo.sgb.gov.br/handle/doc/21828> / (accessed on 7 January 2025)
- Silveira V.D., Gasparotto W., Gonçalves G.F. 2021. Jaguar Mining. *Geologic map of MTL region*. Belo Horizonte. Escala 1:25.000.
- Silveira V.D., Gonçalves G.F.; Brando Soares M., Souza, M.O.A., Massucatto A.J. 2023. Remobilização e reconcentração aurífera associada à tectônica paleoproterozóica: estudo de caso do depósito Faina, Greenstone Belt Pitangui, Minas Gerais. In: Simpósio Brasileiro de Metalogenia, 5, 39. Available online at: [www.ufrgs.br/sbm2023/sites/default/files/anexospagina/anais-v-sbm-2023.pdf](http://www.ufrgs.br/sbm2023/sites/default/files/anexospagina/anais-v-sbm-2023.pdf) / (accessed on 7 January 2025)
- Simmard M., Gaboury D., Daigneault R. 2013. Multistage gold mineralization at the Lapa mine, Abitibi Subprovince: insights into auriferous hydrothermal and metasomatic processes in the Cadillac-Larder Lake Fault Zone. *Mineralium Deposita*, 48, 883-905. <https://doi.org/10.1007/s00126-013-0466-3>
- Swash P.M. 1988. A mineralogical investigation of refractory gold ores and their beneficiation, with special reference to arsenical ores. *Journal of the South African Institute of Mining and Metallurgy*, 88, 173-180. Available on line at: <https://www.saimm.co.za/Journal/v088n05p173.pdf> / (accessed on 7 January 2025)
- Teixeira W., Carneiro M.A., Noce C.M., Machado N., Sato K., Taylor P.N. 1996. Pb, Sr and Nd isotope constraints on the Archaean evolution of gneissic-granitoid complexes in the southern São Francisco Craton, Brazil. *Precambrian Research*, 78, 151-164. [https://doi.org/10.1016/0301-9268\(95\)00075-5](https://doi.org/10.1016/0301-9268(95)00075-5)
- Teixeira W., Ávila C.A., Dussin I.A., Corrêa Neto A.V., Bongioiolo E.M., Santos J.O., Barbosa N.S. 2015. A juvenile accretion

- episode (2.35–2.32 Ga) in the Mineiro belt and its role to the Minas accretionary orogeny: Zircon U–Pb–Hf and geochemical evidences. *Precambrian Research*, 256, 148–169. <https://doi.org/10.1016/j.precamres.2014.11.009>
- Teixeira W., Oliveira E.P., Marques L.S. 2017. Nature and Evolution of the Archean crust of the São Francisco Craton. In: Heilbron M.; Cordani U.G.; Alkmim F.F. (eds.). *São Francisco Craton, eastern Brazil: tectonic genealogy of a miniature continent*. New York, Springer, 29–56. [https://doi.org/10.1007/978-3-319-01715-0\\_3](https://doi.org/10.1007/978-3-319-01715-0_3)
- Vaughan J.P. 2004. The process mineralogy of gold: the classification of ore types. *JOM*, 56, 46–48. <https://doi.org/10.1007/s11837-004-0092-8>
- Vaughan J.P., Kyin A. 2004. Refractory gold ores in Archean greenstones, Western Australia: mineralogy, gold paragenesis, metallurgical characterization and classification. *Mineralogical Magazine*, 68, 255–277. <https://doi.org/10.1180/0026461046820186>
- Vial D.S, Abreu G.C., Schubert G., Ribeiro-Rodrigues L.C. 2007. Smaller gold deposits in the Archean Rio das Velhas greenstone belt, Quadrilátero Ferrífero, Brazil. *Ore Geology Reviews*, 32, 651 – 673. <https://doi.org/10.1016/j.oregeorev.2005.01.004>
- Wang H.; Lan T.; Chen Y.; Hu H.; Shu L. 2022. Mobilization of Au and Ag During Supergene processes in the Linglong Gold deposit: evidence from SEM and LA-ICP-MS Analyses of Sulfides. *Minerals*, 12, 367 p. <https://doi.org/10.3390/min12030367>
- Zalán P.V., Romeiro-Silva P.C. 2007. Proposta de mudança significativa na coluna estratigráfica da Bacia do São Francisco. In: *Simpósio de Geologia do Sudeste*, 10, Programação e Livro de Resumos, 96.